
A SECONDARY PION BEAM FOR THE HADES EXPERIMENT

TECHNICAL DESIGN REPORT
2013

EDITED BY

J. BIERNAT¹, E. EPPLE², L. FABBIETTI², I. FRÖHLICH³,
T. HENNINO⁴, W. KÖNIG³, H. KUC⁴, R. LALIK², P. LOUIS²,
L. MAIER⁵, R. MÜNZER², J. PIETRASZKO³, B. RAMSTEIN⁴,
P. SALABURA¹, T. SCHMITT², E. SCHWAB³, J. SIEBENSON²,
M. TRAXLER³ AND J. WIRTH²

¹*Instytut Fizyki im. Mariana Smoluchowskiego, 30-059 Kraków, Poland*

²*Excellence Cluster 'Origin and Structure of the Universe', 85748 Garching, Germany*

³*GSI Helmholtzzentrum für Schwerionenforschung GmbH, 64291 Darmstadt, Germany*

⁴*Institut de Physique Nucléaire (UMR 8608), CNRS/IN2P3 - Université Paris Sud, F-91406 Orsay Cedex, France*

⁵*Physik Department E12, Technische Universität München, 85748 Garching, Germany*



2013
HADES COLLABORATION
VERSION: 2014/01/28

Contents

1	Physics Case	1	4.2	Experimental Setup	18
1.1	Technical inputs	1	4.2.1	Conclusion and Outlook	19
1.2	Strangeness production in π^- -nucleus reaction	1	4.3	Indirect cooling	20
1.3	Measurements of charged hadrons in an energy scan of the reaction π^-p	3	4.3.1	"Fridge"	20
1.4	Measurement of the reaction π^-p into K-Y channels	4	4.3.2	Experimental setup	21
1.5	Measurements of the reaction $\pi^-p \rightarrow ne^+e^-$ at 0.8 GeV/c	5	5	Mechanical Structure	23
2	Pion Chicane and Beam Optics	6	5.1	Vacuum Chamber	23
2.1	Optimisation of the GSI pion beam line for the HADES experiment	6	5.1.1	Feed-through boards	23
2.1.1	Maximization of the pion beam flux	7	5.1.2	Vacuum feed-through for cooling	24
2.1.2	Measuring the pion momentum	8	5.2	Testing procedure	24
2.1.3	Determination of the pion coordinate at the HADES target point	9	5.3	Chamber mounting	24
2.1.4	Beam profiles	9	6	Front-End and Readout Electronics	26
2.1.5	Beam Purity	10	6.1	The n-XYTER Readout	26
2.1.6	Transport coefficients	11	6.1.1	Front-End Board	27
2.1.7	Impact on the exclusive channels	11	6.1.2	HV Adapter Module	27
2.1.8	Solving the 4 equations	11	6.1.3	Front-End Cooling	27
3	Silicon Detector	13	6.2	Integration of the n-XYTER to the HADES DAQ	27
3.1	Silicon Sensors	13	6.2.1	The TRB3	27
3.1.1	Energy Resolution	13	6.2.2	n-XYTER Front-End Firmware	28
3.1.2	Detector Efficiency	14	6.2.3	The Current Stage of Development	28
3.2	Energy deposition in thin detector layers	15	6.2.4	Readout/DAQ Performance Test	29
3.2.1	Impact on the Pion Tracker performance	15	7	Beam Results	30
4	Detector Cooling	17	7.1	General readout test at FOPI@GSI	30
4.1	Thermal simulation	17	7.1.1	Low trigger rate data	31
			7.2	Beam Results conclusions	33
			8	Start Detector	35
			8.1	Diamond Start Detector Array	35
			8.2	Start detector design	35
			8.3	Current Status	35

Chapter 1

Physics Case

The four following aspects will be covered by the experiment with the GSI pion beam and the HADES[1] spectrometer:

- Strangeness (K^\pm , K_S^0 and ϕ) production in pion-nucleus reactions at a pion momentum $p_\pi = 1.7$ GeV/c.
- One and two-pion channels in π^-p reactions within a scan covering the center-of-mass range between 1.48 GeV ($p_\pi = 0.67$ GeV/c) and 2.1 GeV ($p_\pi = 1.87$ GeV/c).
- Kaon-Hyperon production in π^-p reactions within a scan covering the center-of-mass energy range between 1.61 GeV ($p_\pi = 0.9$ GeV/c) and 2.1 GeV ($p_\pi = 1.87$ GeV/c).
- Study of $\pi^-p \rightarrow ne^+e^-$ reactions below the ω threshold at $\sqrt{s} = 1.55$ GeV ($p_\pi = 0.8$ GeV/c)

1.1 Technical inputs

In 2005, a pion flux of 2.7×10^{-5} π^- per incident N_2 ion beam has been measured in front of the HADES target point, hence giving a lower limit of the pion flux at the exit of the last Q-pole. According to beam optics (see section 2.1.1) calculations, this number should depend only slightly on the tuning of the beam line, the acceptance up to the exit of this last Q-pole being mainly determined by the geometry of the first elements. The size of the beam at the HADES target however depends strongly on the optimization of the beam line and on the vertical alignment of the primary beam. In the optimized set-up, the fraction of the beam at the exit of this last Q-pole which will be inside the 6 mm radius LH2 target is about 2/3.

These numbers have been combined with the primary beam intensity measured by FOPI 8×10^{10} ions/spill (20% higher than in the HADES measurement), corresponding to 60% of the space charge limit.

A 4 s total spill length, based on the choice of a 2 s extraction beam time is most suited to reduce the load on the detectors and the dead time, which leads to an average pion intensity of 3.6×10^5 s $^{-1}$.

Estimates have been made for a 5 cm long liquid hydrogen target, corresponding to 0.72% interaction probability for a beam momentum of 1.7 GeV/c or a 2.5% interaction solid targets, a 30% acquisition dead time and a 80% data taking efficiency. All these numbers are conservative, but the room for improvement, due to the possible use of a 1 s extraction, the increase of the primary beam intensity closer to the space charge limit or the increase of the pion flux in the HADES cave due to a better focus of the beam line is limited to 30–50% at maximum.

1.2 Strangeness production in π^- -nucleus reaction

The production of strangeness in pion- proton- and photon-induced reactions has been already pursued to some extent in recent experiments with the main focus on the study of the properties of K_S^0 , K^+ [2, 3] and ϕ [4, 5] in cold nuclear matter. From the one hand side the real part of the interacting potential between kaons (K_S^0 , K^+) and nucleons has been extracted by comparing the ratios of the momentum distributions obtained in π^- - or p-Pb to π^- - or p-C reactions with transport models. Indeed, due to the expected repulsive potential, a depletion of the low momenta component of the ratio of the momentum distribution for kaons produced off the heavier target respect to the lighter one is expected. The effect of kaon repulsion is more visible for the larger nucleus, where the radius is larger than the average kaon-nucleus mean free path ($\lambda \approx 5$ fm). The so far obtained results show the importance of accessing the low component of the p_T distribution, and is only partially realised in previous experiments, because of the limited acceptance of the employed spectrometer[2, 3]. Moreover the statistics of measured kaons amounts in both experiment to few thousand candidates. The use of pions as primary beams should also facilitate the modelling of the reaction, being the pion absorption on the surface of the nucleus very probable as it is predicted by models and also verified experimentally by the $A^{2/3}$ dependency of the kaon production off different targets[2]. Photon- and proton-nucleon reactions 'happen' through the whole

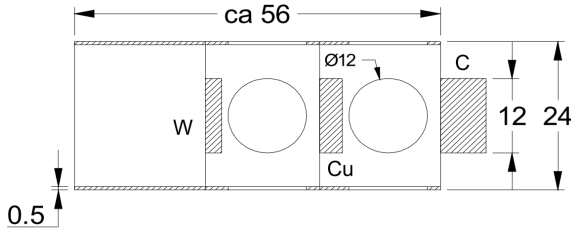


Figure 1.1: Technical drawing of the proposed target ladder with 3 targets which length is chosen such to correspond to 2.5% interaction. Dimension in the figure are in mm.

length of the traversed nucleus, generating secondary processes and resulting in a more complex reaction to be modelled. Following this line, one of the goals of these planned experiments with pion beams is to measure with high statistics the production of K_S^0 , K^+ off C, Cu and Pb nuclei. The beam momentum can range between 1.15–1.65 GeV/c that represent the K_S^0 and ϕ production threshold off a nucleon respectively.

The second goal of the pion-nucleus measurements deals with absorption studies for ϕ and K^- mesons in cold nuclear matter. Following an idea proposed in [6] experimental findings of the absorption of the ϕ meson in cold nuclear matter have been interpreted by theory as the proof of the widening of the ϕ natural width in the medium (from 4 MeV up to 60 MeV).

The dependency of ϕ meson attenuation on mass number (A) is governed by the imaginary part of the ϕ in-medium self-energy or width. In the low-density approximation[7], this width can be related to an effective ϕN absorption cross section $\sigma_{\phi N}$. It is clear that this approximation is not valid at higher densities where two-nucleon effects might be significant. The measurement of the ϕ absorption off different nuclei with an incoming pion beam has never been carried out

yet and it is for sure an important benchmark to shed more light on phi meson in-medium properties. One has to add that this kind of measurements represent to this end one of the very few hints about modification of the intrinsic hadron properties in an environment with finite baryonic density.

Beyond the measurement of the ϕ production in pion-nucleus reaction, also K^- can be addressed. If one considers the microscopic optical potential which is used to explain the wealth of existing data points measured for kaonic atoms[8] a similar study as the one done for ϕ can be carried out. In the case of the K^- constraints to these kind of theories, that also rely on the low density approximation, are to be found in scattering experiments and kaonic-atoms data. The imaginary part of the used potentials is still rather unknown and depends on the role played by 1- and 2- nucleons absorption. It is clear that experimentally it is not so easy to separate these two contributions, but by comparing the yield of kaons and antikaons produced off different nuclei, the total absorption rate for antikaons can be tagged. This is the second and most important goal of the pion-induced measurement related to the strangeness program.

First simulations have been carried out to estimate the feasibility of the aforementioned measurements and the expected count rates per day. A scenario has been investigated where a target ladder with three different layers is put in place.

Figure 1.1 shows the technical drawings of the target ladder with three disks which length corresponds to 2.5% interaction for the Carbon, Copper and Tungsten materials respectively. The distance between the disks is maximised compatibly with the dimensions of the target region. GiBUU simulations of the reactions $\pi^- + C$, $\pi^- + Cu$, $\pi^- + W$ have been carried out for a incoming pion momentum of 1.65 GeV/c and a full scale monte carlo simulation followed by a realistic anal-

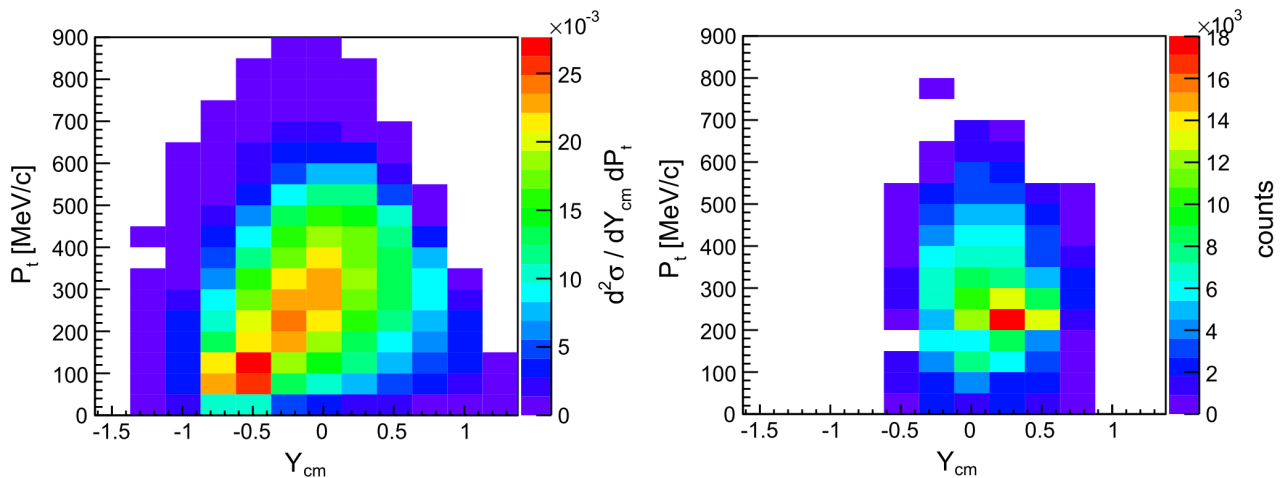


Figure 1.2: p_T versus rapidity distribution of the simulated K_S^0 as the emerge from the GiBUU simulations (left panel) and after the full scale analysis including all the cuts (right panel).

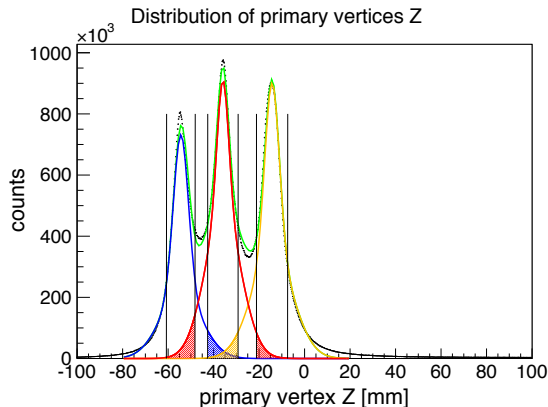


Figure 1.3: Primary target distribution obtained with three targets. The tails of the coloured Gaussian fits show the relative contamination of the different targets to one another.

ysis, which included all the topological and PID cuts normally used for the experimental data, have been executed. Figure 1.2 shows the P_T versus rapidity distribution of the simulated K_S^0 resulting from the GIBUU simulations (left panel) and after the full scale analysis including all the cuts (right panel). One can see that the acceptance of the low P_T part of the spectrum is excellent.

Due to the finite primary vertex resolution, a certain mixing of the reconstructed particles stemming from different targets occurs. This contamination has been estimated via the above mentioned full-scale simulations and fig. 1.3 presents the Z -coordinate distribution of the reconstructed vertices (black line) together with 3 simultaneous Gaussian fits to the distribution (blue, red and yellow curves). The green curve show the sum of the 3 Gaussian distribution. The vertical lines shows the cuts applied in the Z -coordinate to

Table 1.1: Expected event rate per day for strange channels in π^- induced reactions on nuclear targets at $p_\pi = 1.7 \text{ GeV}/c$.

Target	Particle	Rate/day
Carbon	K_S^0	5×10^5
	K^+	5×10^5
	K^-	3×10^4
	ϕ	252
Copper	K_S^0	4.1×10^5
	K^+	5.8×10^5
	K^-	4×10^5
	ϕ	756
Tangsten	K_S^0	2.2×10^5
	K^+	3.4×10^5
	K^-	1.4×10^4
	ϕ	680

select the three different vertices and the tails of the Gaussian fits which extend to the neighbouring target coordinate gives a measure of the contamination.

The count rate estimates per day (24 h) for measurements assuming the intensities and scaling factors mentioned in section 1.1 of the inclusive production of K_S^0 , K^- , K^+ and ϕ are given in table 1.1. One can see that even considering rather conservative estimation for the interaction rates, high statistics is achieved.

Table 1.2 shows the contamination to each particle species for the three different targets stemming from particles produced in other targets. One can see that the contamination level is particularly bad for the central target and hence an independent measurement of the three targets separately is preferable. This scenario has been tested via simulation to check whether a single setting containing the three solid target would have been feasible, in order to minimise the breaks during the data taking. As it is shown, this option seems not very practicable.

1.3 Measurements of charged hadrons in an energy scan of the reaction $\pi^- p$

The baryonic resonances properties are deduced from Partial Wave Analysis (PWA) of both photon and pion induced reactions. While the photon data base has been recently enormously enriched thanks to the experiment at Mainz and Jlab, the pion reaction data base mostly rely on very old and scarce measurements. Being the largest inelastic channel, the two-pion production channel is particularly important, but also the elastic channels would need to be measured with an increased statistics in order to provide better constraints for PWA results concerning resonances with a small pion coupling, like the controversial $P_{11}(1710)$.

Estimates have been done using cross-sections from the SAID data base, of the order of 4–6 mb for the $\pi^- p \rightarrow p\pi^-\pi^0$ and 6–11 mb for the $\pi^- p \rightarrow n\pi^+\pi^-$

Table 1.2: Contamination to each particle species stemming from other targets.

Target	Particle	Contamination
Carbon	K_S^0	5.8 %
	K^+	3.7 %
	K^-	2.0 %
Copper	K_S^0	16.4 %
	K^+	20.1 %
	K^-	9.8 %
Tangsten	K_S^0	1.3 %
	K^+	1.1 %
	K^-	0.8 %

Table 1.3: Typical cross-sections for the $\pi^-p \rightarrow p\pi^-\pi^0$ and $\pi^-p \rightarrow n\pi^+\pi^-$ reactions in the centre of mass energy range between 1.48 and 2.1 GeV, expected total count rate per hour and average yield for one shift in one of the 8000 bins (20 bins in each of the two π -N invariant masses and 20 bins in $\cos\theta_{\pi\pi}$).

	$\pi^-p \rightarrow p\pi^-\pi^0$	$\pi^-p \rightarrow n\pi^+\pi^-$
σ [mb]	4.8	8
evts/hour	95000	130000
evts/bin/shift	95	130

channel. The combined effect of acceptance and efficiency for the measurement of the two charged particles in the HADES detector is of the order of 15 to 20 % for both channels, with small dependence on the energy. The use of the Forward Wall has not yet been studied, but could increase significantly the acceptance.

Using pion momenta between 0.67 and 1.87 GeV/c, centre of mass energies between 1.48 and 2.1 GeV can be accessed. Typical count rates for a measurement at a given setting are 95 000 evts/h for the $\pi^-p \rightarrow p\pi^-\pi^0$ channel and 130 000 evts/h for the $\pi^-p \rightarrow n\pi^+\pi^-$ channel (table 1.3). Using 20 bins in each of the two πN invariant masses as well as 20 bins in $\cos\theta_{\pi\pi}$ (8000 bins in total), about 0.8 shift, where one shift corresponds to 8 hrs of data taking, for each point will be needed to measure about 80 counts for the $\pi^-p \rightarrow p\pi^-\pi^0$ reaction and 110 for the $\pi^-p \rightarrow n\pi^+\pi^-$ reaction, which should be enough for precise Partial Wave Analysis. With 7 days of beam time, 26 points can be measured. With a spacing of about 25 MeV, this allows for a precise scan in the range $1.48 \leq \sqrt{s} \leq 2.105$ GeV.

In fact, the time devoted to each measurement and the spacing of the energy steps will be tuned in order to get a similar statistics in each energy bin taking into account the smooth evolution of the cross-section and the momentum acceptance of the beam line. The overlap between the momentum acceptance of two settings will be used to minimize systematic errors on the normalization of the measurements. For a given setting, the distribution of pion momenta at the target is asymmetric, with 95 % of the pions between -2.5% and 3.5% with respect to the central value. The corresponding range in center of mass energy is 26 MeV for $\sqrt{s} = 1.48$ GeV and 51 MeV for $\sqrt{s} = 2.1$ GeV, allowing for bigger steps at the highest energies.

The average numbers given above corresponding to 0.8 shift per energy point are sufficient to show the potential of the measurement with HADES: in total 21×10^6 events can be measured for the $n\pi^+\pi^-$ channel and 15×10^6 events in the $p\pi^-\pi^0$ channel, to be compared to the existing database of respectively 114×10^3 and 72×10^3 events.

Elastic ($\pi^-p \rightarrow \pi^-p$) channels are measured simultaneously. The combined effect of acceptance and efficiency for one particle being detected in HADES is

Table 1.4: Expected number of counts for strange exclusive channels in the reaction π^-p per day and an incident pion momentum $p_\pi = 1.7$ GeV/c. E and SE refers to the exclusive and semi-exclusive analysis respectively, see text for details.

$\pi^-p \rightarrow$	$\Sigma^- K^+$	ΛK_S^0	$\Sigma^0 K^0$
events/day E	24000	900	700
events/day SE	—	6500	5000

about 66 % and amounts to 55 % for the detection of both particles. For each energy point, 6×10^6 events to 15×10^6 events can be measured, allowing for very precise angular scattering measurements.

1.4 Measurement of the reaction π^-p into K-Y channels

Analog to the coupling of the π^-p initial state to 1 or 2-pion resonant state, a similar analysis can be carried out looking at the kaon-hyperon final state. On the one hand side the coupling of the elementary reaction to kaons and hyperons is a fundamental input for the correct modelling of secondary reactions in heavy ion collisions by transport models. On the other hand the search or resonant system in the kaon-hyperon channels has been suggested by theoretical predictions. For example, with a pion beam of 1.7 GeV/c and $\sqrt{s} = 2.026$ GeV one is about 20 MeV above the threshold of $K^*\Lambda$. This reaction is interesting because there is a resonance around 1.9 GeV that could couple very strongly to the $K^*\Lambda$ final state resulting in a increased cross section close to threshold[9]. To begin with, the following exclusive channels have been simulated in parallel to the pionic channels in the energy scan measurements when the pion momentum is above the corresponding threshold:

- $\pi^-p \rightarrow \Sigma^- K^+$ for $p_\pi > 1.035$ GeV/c, with all decay particles detected in HADES but the neutron.
- $\pi^-p \rightarrow \Lambda K_S^0$ for $p_\pi > 0.896$ GeV/c, with all decay particles detected in HADES and for only the K_S^0 in the acceptance.
- $\pi^-p \rightarrow \Sigma^0 K^0$ for $p_\pi > 1.031$ GeV/c, with all decay particles detected in HADES but the photon and photon plus K_S^0 identified.

The exclusive analysis (E) assumes that all the charged particles are identified in the HADES acceptance and a PID of about 95 % purity is used for the TOF determination together with a 90 % purity per particle for the dE/dx selection of charged hadrons. The analysis of the reaction $\pi^- + p \rightarrow \Sigma^- + K^+$ relies on the kinematical refit of the missing neutron mass. For the analysis of the channel $\pi^- + p \rightarrow \Lambda + K^0$ the

exclusive analysis (E) assume the identification of the Λ and K_S^0 weak decays into charged particles, while the semi-exclusive (SE) analysis, assume that only the K_S^0 is identified and a kinematical refit to its mass is applied to reject background. In the case of the reaction $\pi^- + p \rightarrow \Sigma^0 + K^0$, the same procedure as for the $\pi^- + p \rightarrow \Lambda + K^0$ reaction is applied, adapting the cuts to the fact that a photon is missing. The expected count rates for an incident pion beam of 1.7 GeV/c recorded per day, according to the beam intensity and dead time assumed in section 1.1, are listed in table 1.4.

1.5 Measurements of the reaction $\pi^- p \rightarrow ne^+e^-$ at 0.8 GeV/c

The study of the exclusive $\pi^- p \rightarrow ne^+e^-$ reaction below the ω threshold offers a unique possibility to measure the coupling of baryonic resonances to off-shell vector mesons, which is of crucial importance for the understanding of medium effects in hadronic matter. These couplings are indeed thought to be at the origin of the in-medium modifications of the vector meson spectral function in hadronic matter.

The contribution of baryonic resonances to the $\pi^- p \rightarrow ne^+e^-$ reaction can be described in two ways. In a first approach, the baryonic resonance first decay into a ρ or ω meson which subsequently decays into an e^+e^- pair. In a second approach, a Dalitz decay ($R \rightarrow ne^+e^-$) of the baryonic resonance R is considered and time-like electromagnetic form factors, taking into account the electromagnetic structure of this baryonic transition have to be introduced. When using Vector Dominance Model form factors, the two approaches are equivalent.

The feasibility of the measurement of the reaction $\pi^- p \rightarrow ne^+e^-$ with HADES has been performed for an incident pion momentum $p_\pi = 0.8$ GeV/c, corresponding to $\sqrt{s} = 1.55$ GeV. In this energy range, different resonances can be excited, the most important being $N^*(1440)$, $N^*(1520)$ and $N^*(1535)$.

The choice of $p_\pi = 0.8$ GeV/c was made due to the existing calculations for this energy of [10] based on the coupling of vector mesons to baryonic resonances. A spectacular destructive interference between the iso-scalar (off-shell ω) and the iso-vector (off-shell ρ) has been predicted, with a maximum effect at $\sqrt{s} = 1.55$ GeV, where an almost total cancellation of both contributions occurred. Calculations based on the same approach, but with different couplings[11], showed the same qualitative trends, with however larger cross sections. More recent calculations have been performed using VDM form factors[12], where the contribution of vector mesons is not described explicitly, but is embedded in the VDM form factors.

Events from the reaction $\pi^- p \rightarrow ne^+e^-$ can be identified using missing mass cuts. The uncertainty on the incident pion beam momentum deduced from the po-

Table 1.5: Expected number of counts with e^+e^- invariant mass larger than 140 MeV/c² for the $\pi^- p \rightarrow ne^+e^-$ reaction at an incident pion beam momentum $p = 0.8$ GeV/c and for two weeks of beam time. The cross-sections are taken from a resonance model (first column), the model of ref.[10] (second column), and the model of ref.[11] (third column).

	resonance model	model from [10]	model from [11]
evts./two weeks	1840	≈ 200	≈ 6000

sitions in the Si tracker has a much smaller contribution to the missing mass resolution than the momentum resolution of the particles detected in HADES. The remaining contribution of η Dalitz decay ($\eta \rightarrow \gamma e^+e^-$) is negligible. However, the π^0 Dalitz decays ($\pi^0 \rightarrow \gamma e^+e^-$) can not be fully rejected. Therefore the reaction can only be measured for the invariant e^+e^- mass larger than 140 MeV/c², in the same way as for the $pp \rightarrow ppe^+e^-$ reaction, already studied by HADES.

Estimates have been made using a resonance model and taking into account the acceptance and efficiency of HADES detector. The dilepton yield was calculated as an incoherent sum of the contributions from the different resonances in the two-step process $\pi^- + p \rightarrow R \rightarrow ne^+e^-$. The production cross section of each resonance was deduced from the partial decay width towards the πN channel and the Dalitz decay width has been calculated using Zetyenyi and Wolf parametrization[13] with constant electromagnetic form factors adjusted to reproduce the radiative decay width of the resonances.

Within this simple model, 1840 e^+e^- pairs are expected for two weeks of beam time, with an invariant mass larger than 140 MeV/c² (see table 1.5). As a complement to the e^+e^- mass distribution, the measurement of the helicity angle distribution (angle of one lepton in the e^+e^- reference frame, with polar axis along the centre of mass momentum) will bring useful constraints on the contribution of the different resonances and their electromagnetic couplings.

Simulations have also been performed using calculations of ref.[10]. Due to the very strong destructive interference between both contributions, a very small yield is predicted, about a factor 10 smaller than in our resonance model estimates. In the model of [11], the cross-sections around $\sqrt{s} = 1.55$ GeV are roughly a factor 30 higher than with the model of ref.[10]. In the more recent model by Zetyenyi and Wolf based on VDM form factors[12], a cross-section of the same order is found, without including any contribution from the ω meson. The very large scattering of these predictions is due to the bad knowledge of the coupling of baryonic resonances to off-shell mesons and/or to the unknown electromagnetic form factors in the time-like region. The measurement with HADES of the $\pi^- p \rightarrow ne^+e^-$ will clearly be able to bring quantitative constraints.

Chapter 2

Pion Chicane and Beam Optics

2.1 Optimisation of the GSI pion beam line for the HADES experiment

As a secondary beam, the properties of pion beams are quite different from primary beams. In the first step, pions are produced by the interaction of an intense beam on a thick target. The outgoing spectrum is widely open both in momentum and in angle. The momentum and the nature of the primary beam, as well as the production target geometry and nature determine the pion momentum distribution. The best compromise for pion beam momentum in the 1 GeV/c regime was shown to be given by a 2 GeV per nucleon fully stripped ^{12}C or ^{14}N ion beams at the SIS18 charge space limit impinging on a 10 cm thick Be target. In order to reach significantly higher pion momenta, it is necessary to increase the incident momentum and then to consider a primary proton beam. The optical and geometrical properties of the spectrometric line which transports the pions to the HADES target entirely define the fraction of pions reaching the HADES target as well as their momentum and angular distributions. For that reason it is essential to find the best parameters which maximize the secondary beam quality at the HADES target.

There are four items which should be studied

- How to maximize the flux of pions on the HADES target, located about 33.5 m downstream from the production target.
- How to provide a mean to measure individually the vector momentum of each individual pion in the beam.
- What is the fraction of the pion beam that fulfil the conditions imposed by the liquid hydrogen target (LH2) inner beam pipe size and by the Diamond start detector.
- What is the purity of the pion beam.

For these studies, a Monte Carlo simulation was carried out. The full calculation is done in 2 steps. In the first step, a Transport program code[14] is used to

tune the quadrupoles strengths and positions (only for those that can be moved along the optical axis, i.e. in the HADES cave) in such a way to ensure focus at the intermediate image and focus + achromaticity at the final HADES target point in both vertical and horizontal directions. A description of the line by first and second order coefficients is then obtained and fed in a event by event based Monte Carlo simulations where each particle is traced all along the spectrometer within the geometrical acceptance of the quadrupoles and dipoles.

In the usual Transport notation and in the absence of acceleration devices, one uses 5 variables to describe the coordinates of a particle with momentum p in an x-y plane perpendicular to the optical axis of the system, taken as the z-axis and corresponding to central momentum p_{spec} :

- x , the x coordinate, referred to with the index 1,
- θ , the horizontal angle, defined by $\tan(\theta) = dx/dz = p_x/p_z$, referred to with the index 2,
- y , the y coordinate, referred to with the index 3,
- φ , the vertical angle, defined by $\tan(\varphi) = dy/dz = p_y/p_z$, referred to with the index 4,
- δ , the momentum offset $\delta = (p_\pi - p_{\text{spec}})/p_{\text{spec}}$, referred to with the index 6.

The standard units used in Transport calculations are cm for position variables (x or y), mrad for angles (θ or φ) and % for momentum offset δ .

The excursion of a particle emitted at the production target with the initial conditions $x_0, \theta_0, y_0, \varphi_0$ and δ can then be calculated using the formula:

$$x_i = \sum_{j=1,6} T_{ij} \cdot x_j + \sum_{\substack{j=1,6 \\ k=j,6}} T_{ijk} \cdot x_j x_k$$

where

$$x_{i;i=1,2,3,4,6} = x_0, \quad \theta_0, y_0, \quad \varphi_0, \quad \delta$$

The T_{ij} coefficients represent the first order terms while the T_{ijk} coefficients represent the second order

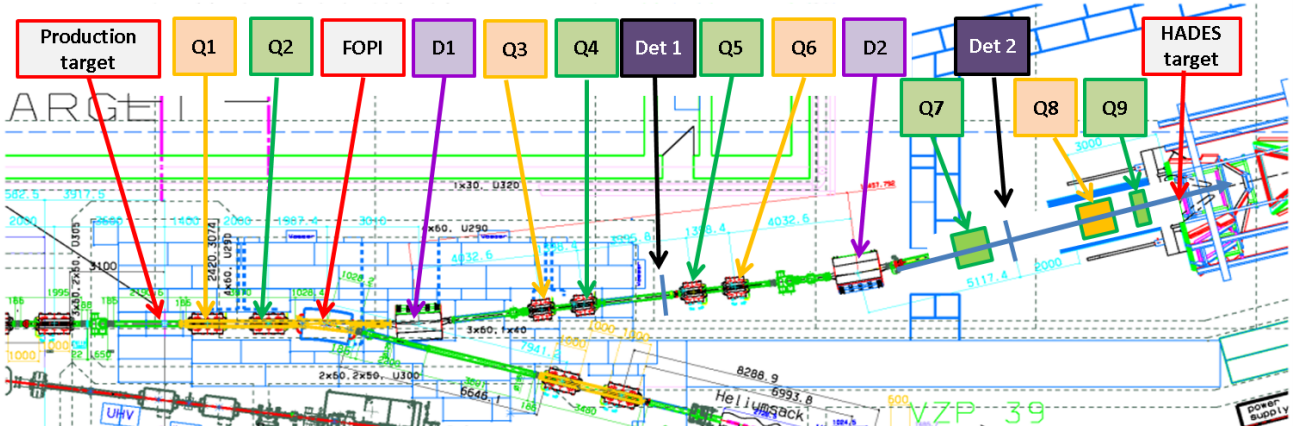


Figure 2.1: Technical drawing of the top view of the part of GSI beam line, between the pion production target and the HADES cave. All detectors, magnets and elements included in the transport simulations are indicated.

ones, which carry the information on the geometrical and chromatic aberrations. In the case of the HADES beam line, the distributions at the production target were taken to be Gaussian-like for x_0 and y_0 with a typical rms value of 0.5 mm and uniform for θ_0 ($\Delta\theta_0 = \pm 10$ mrad), φ_0 ($\Delta\varphi_0 = \pm 50$ mrad) and δ ($\delta = \frac{\Delta p}{p} = \pm 6\%$). The geometrical limitations imposed by the size of the vacuum pipes all along the beam transport line were taken into account by requiring that at each step (input and output of each element, dipole, Q-pole, drift length, etc...) the excursion of a particle from the optical axis stays within the corresponding limits. As position sensitive detectors are inserted in the beam line, the effect of multiple scattering in the first detector material and the detector position resolution were also taken into account.

Provided that the x and y coordinates of each individual pion are measured at two different locations along the beam line, it is possible to relate these quantities to the pion kinematical variables (p_x, p_y, p_z) (or equivalently p, θ, φ) at the pion production target or at any place in the beam line.

2.1.1 Maximization of the pion beam flux

Given the primary pion flux at the production target, emitted in the entire phase space, one then has to maximize the fraction of this primary flux which reaches the HADES target. Figure 2.1 shows the HADES beam line. A third quadrupole (40 cm long) was recently added in the HADES beam cave to help in obtaining the best focusing conditions at the HADES target. Besides the 6 first quadrupoles of the beam line, which cannot be moved any more, we do have at our disposal 3 quadrupoles which positions can be adjusted freely in the HADES cave, labelled Q7 to Q9. The optimization of the beam line was then made by fulfilling the 3 following constraints:

- focus in horizontal and vertical planes at both in-

termediate and final images,

- maximal solid angle acceptance,
- achromaticity in both horizontal and vertical planes at the final HADES target point.

Two different scenarios were studied. The first one, corresponding to the standard HADES beam line configuration (Q7 – 1 m long, Horizontal focusing; Q8 – 1 m long, Vertical focusing; Q9 – 0.4 m long, Horizontal focusing) and a second one (Q7 – 0.4 m long, Horizontal focusing; Q8 – 1 m long, Horizontal focusing; Q9 – 1 m long, Vertical focusing). Within these two possible setups, the transmission of the pions produced at the production target is very similar; the relative difference is smaller than 3%. However, the standard setting yields a much narrower beam envelope at the LH2 target entrance window. Almost 100% of the pions fit within the 48 mm diameter of the LH2 inner stainless steel tube, whereas the corresponding figure is only $\approx 60\%$ for the second quadrupole tuning. For this reason, the standard solution is preferred.

The transmission of the different pion momenta is illustrated in fig. 2.2. Whereas the global transmission of pions with $\delta = 0\%$ is close to 56%, the transmission gradually decreases as one goes off the central momentum. The asymmetry between corresponding negative and positive values is due to the second order effects (T_{ijk} terms). The transmission completely dies off above 6%. The overall transmission, for a square distribution ranging from -6% to 6% is about 18.6%. Note however that this number corresponds to the simulation initial conditions with square distributions in all variables that go beyond the transmission of the beam for any quadrupole tuning and that it can only be used for comparing different beam line tunings.

The location of the two position-sensitive detectors was also carefully studied. It is then proposed to install the first one close to the intermediate image with a proper shielding to get rid of the secondaries produced by the impact of the slowed-down beam and

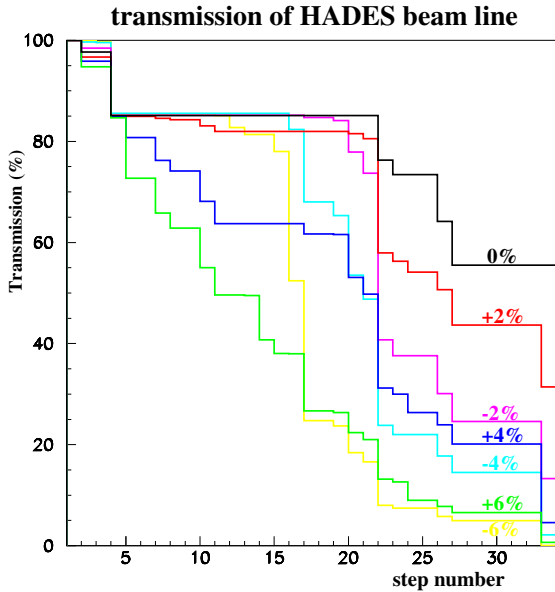


Figure 2.2: Transmission of the pion for 7 different values of δ as a function of the step number. Important cuts appear at different steps. They correspond respectively to cuts imposed by the following constraints: horizontal aperture of the second quadrupole (step 4), vertical aperture of the first dipole (step 11), size of detector 1 (step 17), vertical aperture of the second dipole (step 23), vertical aperture of the 7th quadrupole (step 27) and finally the 6 mm condition at the HADES target (step 33).

fragments in the beam pipe and return yoke of the first dipole. The fine tuning of the detector position does not seem to be an issue, at least as long as the second detector stays between the 7th and the 8th quadrupoles.

The influence of a shift of the primary beam on the production target was simulated. A shift of 0.1 cm along the x-direction immediately translates into a global shift of the whole pion momentum spectrum. The corresponding momentum shift is of the order of 0.22%, as expected from the size of the linear magnification term $T_{11} = -1.78$ and the dispersion term at the intermediate image $T_{16} = -0.813 \text{ cm } \%^{-1}$. The transmission at the HADES target point is only weakly affected as long as the shift stays below 2 mm. The resolution is only marginally affected for $\delta < 4\%$.

The vertical shift has a completely different and complicated behaviour that is driven not only by first order terms, but also by second order terms that couples the vertical coordinate at the production target to momentum. For example, the linear magnification coefficients T_{33} is about -3.0 at the final HADES target point but reaches -16.0 at the intermediate image. For the detector 1, a 1 mm shift at the emission point would shift the central momentum pions by 1.6 cm, i.e. 1/3 of the detector half width. The second order term T_{336} , that couples a vertical shift to δ , reaches values up to 4 mm

for $\delta = 5\%$ at the HADES target. It is then very important to control the beam position at the production target and to carry on some fine tuning for optimization. This can be done by using the kickers and the beam profilers installed on the line before the production target. The shape of the momentum transmission curve for the pions reaching the HADES within the usable area ($|x| \leq 0.6 \text{ cm}$, $|y| \leq 0.6 \text{ cm}$) is then notably affected by a vertical shift, reshuffling the transmission of the different momenta. Overall, the loss amounts to 15% for a vertical shift of 0.05 cm and reaches 50% for 0.1 cm. The transmission curve can be modelled by a Gaussian with a σ value of 0.07 cm.

2.1.2 Measuring the pion momentum

From the measurement of 4 positions X^{det1} , Y^{det1} , X^{det2} and Y^{det2} at the two detectors, neglecting third order effects and neglecting terms which correspond to contributions that are smaller than half the detector resolution, one can simplify the above formula and relate the x and y coordinates of the particle when crossing the two detectors to the quantities at the pion production target, x_0 , θ_0 , y_0 , φ_0 and δ :

$$\left\{ \begin{array}{l} X^{\text{det1}} = T_{11}^{\text{det1}} \cdot x_0 + T_{12}^{\text{det1}} \cdot \theta_0 + T_{14}^{\text{det1}} \cdot \varphi_0 \\ \quad + T_{16}^{\text{det1}} \cdot \delta + T_{116}^{\text{det1}} \cdot x_0 \delta + T_{126}^{\text{det1}} \cdot \theta_0 \delta \\ \quad + T_{146}^{\text{det1}} \cdot \varphi_0 \delta + T_{166}^{\text{det1}} \cdot \delta^2 \\ X^{\text{det2}} = T_{11}^{\text{det2}} \cdot x_0 + T_{12}^{\text{det2}} \cdot \theta_0 + T_{14}^{\text{det2}} \cdot \varphi_0 \\ \quad + T_{16}^{\text{det2}} \cdot \delta + T_{116}^{\text{det2}} \cdot x_0 \delta + T_{126}^{\text{det2}} \cdot \theta_0 \delta \\ \quad + T_{146}^{\text{det2}} \cdot \varphi_0 \delta + T_{166}^{\text{det2}} \cdot \delta^2 \\ Y^{\text{det1}} = T_{32}^{\text{det1}} \cdot \theta_0 + T_{33}^{\text{det1}} \cdot y_0 + T_{34}^{\text{det1}} \cdot \varphi_0 \\ \quad + T_{36}^{\text{det1}} \cdot \delta + T_{336}^{\text{det1}} \cdot y_0 \delta + T_{346}^{\text{det1}} \cdot \varphi_0 \delta \\ \quad + T_{366}^{\text{det1}} \cdot \delta^2 \\ Y^{\text{det2}} = T_{32}^{\text{det2}} \cdot \theta_0 + T_{33}^{\text{det2}} \cdot y_0 + T_{34}^{\text{det2}} \cdot \varphi_0 \\ \quad + T_{36}^{\text{det2}} \cdot \delta + T_{336}^{\text{det2}} \cdot y_0 \delta + T_{346}^{\text{det2}} \cdot \varphi_0 \delta \\ \quad + T_{366}^{\text{det2}} \cdot \delta^2 \end{array} \right.$$

A careful analysis of the role of each of the 5 first order and of the 21 second order terms has been performed. Only the terms giving contributions that are larger than half of the position sensitive detector digitalization step (0.781 mm) have been kept in the above equations. Due to the tilt angle (21.75°) of the two beam line dipoles, horizontal and vertical planes are not separated, giving rise to the non negligible first order coupling terms T_{14} and T_{32} and to the second order ones T_{146} , T_{336} , T_{346} and T_{366} .

This set of 4 equations with 5 unknown can generally be solved by neglecting the smallest contribution. In most cases, the smallest contribution is the one which couples to the horizontal object size, namely x_0 (terms $T_{11}x_0$ and $T_{116}x_0\delta$). The numerical contribution of these terms then determines the resolution on the other quantities θ_0 , y_0 , φ_0 and δ . When horizontal

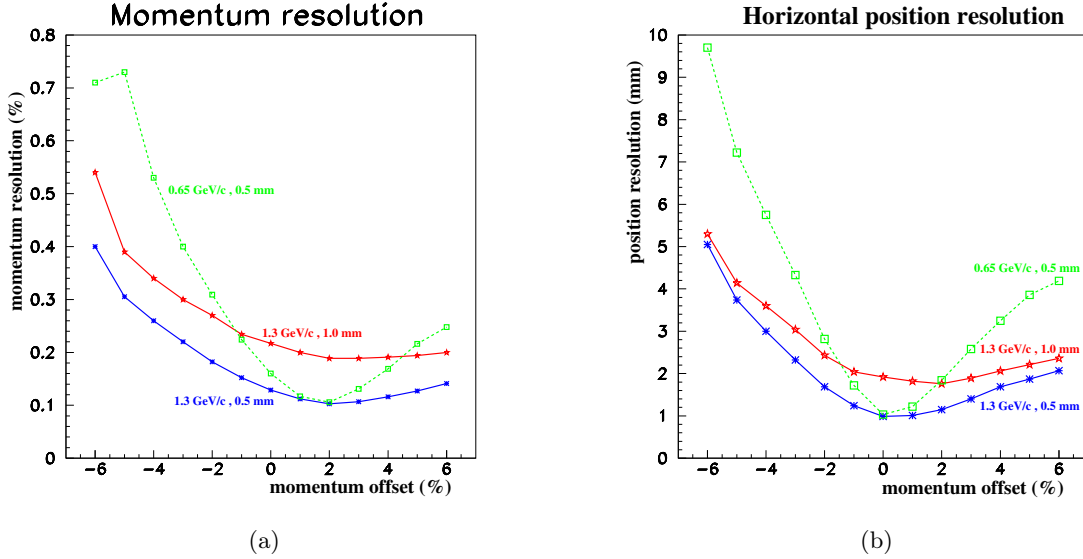


Figure 2.3: (a) Pion momentum resolution against the momentum offset δ . As one runs away from the central momentum ($\delta = 0$), the resolution gets significantly worse and the transmission dies off. (b) Horizontal resolution on the pion impact point at the HADES target (in mm). The blue curve, respectively red, corresponds to the standard beam horizontal spot size of 0.05 cm, respectively 0.1 cm, for $p_\pi = 1.3$ GeV/c. The green curve stands for $p_\pi = 0.65$ GeV/c.

and vertical are not or very weakly coupled, the two first equations allow to determine the quantities θ_0 and δ , the two last equations then providing values for φ_0 and y_0 . In the case of HADES, this is not possible and the set of 4 equations has to be solved iteratively (see section 2.1.8 for a detailed explanation of the solving algorithm, the values of the coefficients).

Figure 2.3a shows the pion momentum resolution against the momentum offset δ for the following initial conditions: x_0 Gaussian distributed with $\sigma_x = 0.05$ cm, θ uniformly distributed within the interval -10 mrad to 10 mrad, y_0 Gaussian distributed with 0.05 cm, φ uniformly distributed within the interval -50 mrad to 50 mrad, δ uniformly distributed within the interval -6% to 6% . For pions travelling along the optical axis, the resolution is about 0.1% . This value grows linearly as a function of the horizontal beam spot size at the production target. If one wants to keep the resolution at this per mil level, it is then mandatory to keep the primary beam transverse size at the target production as small as possible; increasing the beam spot size by a factor 2 results in a worsening of the resolution by a factor 2 for the central momentum (see red curve on fig. 2.3a). The asymmetric behaviour is due to the non linear terms involving coupling between δ and θ_0 or φ_0 . The value of 0.4% at $\delta = -6\%$ corresponds to an extremely weak transmission, much below 0.1% .

2.1.3 Determination of the pion coordinate at the HADES target point

By using the extracted values of θ_0 , y_0 , φ_0 and δ , it is possible to calculate the corresponding Y^H and

Y^H coordinates at the HADES target point and compare them to the generated Monte Carlo values. The resolution on the horizontal impact point, as defined by the distance between the reconstructed one and the true Monte Carlo one is displayed in fig. 2.3b. The resolution is of the order of 1 mm for δ close to 0% , as expected from the value of the linear magnification coefficient $T_{11} = 1.86$ at the HADES target and the horizontal size of the beam at the pion production target $x_0 = 0.05$ cm. For $-2.5\% \leq \delta \leq 3.0\%$, corresponding to 95% of the total pion flux ($\pm 2\sigma$), the X position resolution stays below 2.5 mm. The Y impact resolution is at the level of a few hundred microns, although one has to note that the corresponding resolution pattern is far from Gaussian.

2.1.4 Beam profiles

Figure 2.4a shows the spatial profile of the pion beam at 4 different places for all the pions that reach the HADES target within the usable area (distance to optical axis at the HADES target $-6 \text{ mm} \leq X(Y) \leq 6 \text{ mm}$). The loss of pions through an interaction with the inner LH2 tube, 48 mm in diameter, is fully negligible (see bottom left part of the fig. 2.4a), whereas the loss due to the Diamond detector useful detection area ($14.4 \times 14.4 \text{ mm}^2$) induces a loss of a few % (bottom right part of fig. 2.4a). One clearly sees that the loss of a few channels near the edges of the detectors is also very small (top part of fig. 2.4a). Indeed, the present size and location of the Diamond detector is so that it matches almost perfectly to the HADES LH2 target usable area: the pions which will not have a Diamond

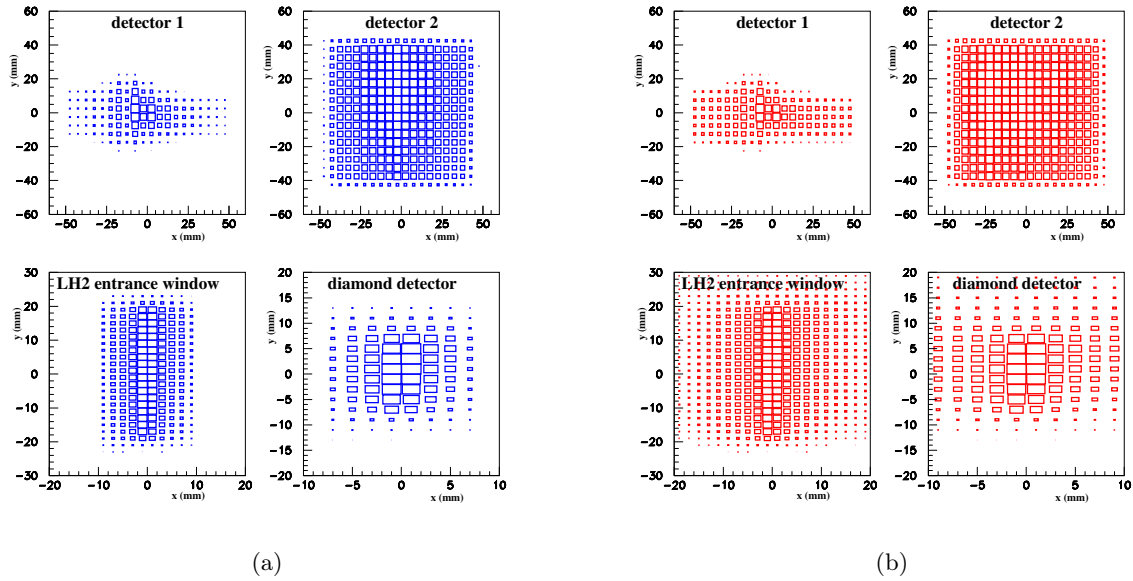


Figure 2.4: (a) X-Y distribution at the first detector (top left), at the second detector (top right), at the entrance of the LH2 inner tube (bottom left) and at the Diamond detector located 40 cm upstream from the HADES target (bottom right) with condition that the pions reach the HADES target within a radius of 6 mm. The z scale, represented by the square size, is linear. The momentum distribution is uniform between -6% and 6% (b) The same but for all pions that emerge out of the last quadrupole Q9. Note in that case that a sizeable fraction of the pions do interact with the LH2 inner tube ($r = 24$ mm) or are not detected by the Diamond detector ($-7.5 \text{ mm} \leq X(Y) \leq 7.5 \text{ mm}$).

detector signature will mostly correspond to pions having either interacted with the LH2 inner tube and/or being outside the usable area. Recent tests have shown that it might be possible, although mechanically tricky, to install the Diamond detector closer to the target, up to 20 cm ahead of target. In these conditions, there will be no loss at all.

Figure 2.4b gives the same distributions for the pions that emerge out of the last quadrupole Q9. Looking at the bottom left plot of the figure, one realizes that a sizeable fraction of the pions that emerge out of the Q9 quadrupole will hit the LH2 inner tube. It is then mandatory to perform GEANT calculations to simulate the effect of this fraction of beam interacting with large amount of material (particle travel almost parallel to the beam tube)

For the central momentum, the distribution of the pions stays well inside the 6 mm condition. When moving away from the central momentum, the distribution gets broader, mostly driven by the second order terms. For off-central momentum, the loss is mostly due to a broadening of the impact distribution in x, the distribution in y staying always within the 6 mm conditions for any momentum.

2.1.5 Beam Purity

For negative pions, the background particles in the beam are electrons, muons and kaons.

The electrons find their origin in the Dalitz decay ($\pi^0 \rightarrow \gamma e^+ e^-$ with $BR = 1.17\%$) of the copiously produced neutral pions at the production target. They are emitted at the production target and due to the 3-body kinematics, only a very small fraction of these electrons will reach the HADES target environment. Due to the low interaction cross section, they do not represent a dangerous background.

The muons stem directly from in-flight decaying pions. Over the path length of the beam line, at $1.4 \text{ GeV}/c$, only 10% of the charged pions will decay, leading to a moderate muon flux at the HADES target. As a general trend the muon momentum distribution at the HADES target will result from two opposite effects, one related to the decrease of the pion decay yield due to the Lorentz factor as the momentum increases, the other being the ability of the beam line to transport (kinematical focusing) a larger fraction of the decay muons. The interaction cross section with matter is also quite low.

The negative Kaons may also be produced through the associate strangeness production reaction $NN \rightarrow NNK^+K^-$. As the kinematical threshold of this reaction is about 2.5 GeV , the production rate is quite low. Furthermore, due to its higher mass, the kaon will have a much lower effective value of the decay length and then most of the Kaons will decay ($c\tau = 3.71 \text{ m}$) before reaching the pion tracking detectors and the final HADES ones.

None of these particles will induce a dangerous background at the HADES target point.

2.1.6 Transport coefficients

All the first order and second order transport coefficients were obtained through the TRANSPORT code. Their correctness relies on the fact that the beam transport line is perfectly modelled by this approach. Imperfections, like misalignments or more complicated fringe field can modify slightly the coefficients. It is then mandatory to realize a few checks with a proton or a heavy ion beam in the GeV/c momentum range while the pion production target is off.

First of all, one has to measure the first and second order dispersive terms T_{16} , T_{36} , T_{166} and T_{366} . Tuning the incident beam line before the pion production target in the standard way (*i.e.* centered in x_0 , θ_0 , y_0 and φ_0), 3 different tunings of the pion beam line, namely -3% , 0% and 3% with respect to the rigidity of the primary should be enough to measure these 4 coefficients. For the coefficients that couple to θ_0 , namely T_{12} , T_{32} , and T_{126} , the incident beam must be tuned at the production target so that the incident beam is centred at $\theta = 5$ mrad. For the coefficients that couple to φ_0 , namely T_{14} , T_{34} , T_{146} and T_{346} , the incident beam must be tuned at the production target so that the incident beam is centred at $\varphi = 10$ mrad.

2.1.7 Impact on the exclusive channels

The impact of the resolution on the kinematical properties (p , θ and φ) of each pion at the HADES target was also estimated. Whereas the role of the angles can be completely neglected, the impact of the pion momentum resolution on the identification of exclusive channels, mostly based on cuts applied to missing mass or invariant mass was estimated for the reaction $\pi N \rightarrow ne^+e^-$ at two different energies, namely 0.8 and 1.3 GeV and for two values of the e^+e^- invariant mass, 0.2 and 0.8 GeV/ c^2 . In both cases, the effect is about a factor 3 below the contribution of the detector resolution.

Table 2.1: Numerical values of the transport coefficients in the horizontal plane at the two detector positions.

Coefficient	Detector 1	Detector 2
T_{11}^{det} [cm/cm]	-1.782	-9.242×10^{-1}
T_{12}^{det} [cm/mrad]	-4.835×10^{-2}	-4.770×10^{-1}
T_{14}^{det} [cm/mrad]	-1.112×10^{-3}	8.200×10^{-5}
T_{16}^{det} [cm/%]	-8.128×10^{-1}	-1.615×10^{-1}
T_{16}^{det} [cm/cm/%]	1.505×10^{-2}	-1.915×10^{-2}
T_{126}^{det} [cm/mrad/%]	3.073×10^{-1}	-3.181×10^{-1}
T_{146}^{det} [cm/mrad/%]	-3.055×10^{-4}	9.178×10^{-4}
T_{166}^{det} [cm/% ²]	5.396×10^{-3}	-2.303×10^{-1}

2.1.8 Solving the 4 equations

Since one cannot extract 5 unknown variables out of the set of 4 equations of section 2.1.2, one usually assumes that the particles are emitted with $x_0 = 0$. The corresponding terms, namely $T_{11}x_0$ and $T_{116}x_0\delta$ are then dropped out. The system of 4 equations reads:

$$\left\{ \begin{array}{l} X^{\det 1} = T_{12}^{\det 1} \cdot \theta_0 + T_{14}^{\det 1} \cdot \varphi_0 + T_{16}^{\det 1} \cdot \delta \\ \quad + T_{126}^{\det 1} \cdot \theta_0\delta + T_{146}^{\det 1} \cdot \varphi_0\delta + T_{166}^{\det 1} \cdot \delta^2 \\ X^{\det 2} = T_{12}^{\det 2} \cdot \theta_0 + T_{14}^{\det 2} \cdot \varphi_0 + T_{16}^{\det 2} \cdot \delta \\ \quad + T_{126}^{\det 2} \cdot \theta_0\delta + T_{146}^{\det 2} \cdot \varphi_0\delta + T_{166}^{\det 2} \cdot \delta^2 \\ Y^{\det 1} = T_{32}^{\det 1} \cdot \theta_0 + T_{33}^{\det 1} \cdot y_0 + T_{34}^{\det 1} \cdot \varphi_0 \\ \quad + T_{36}^{\det 1} \cdot \delta + T_{336}^{\det 1} \cdot y_0\delta + T_{346}^{\det 1} \cdot \varphi_0\delta \\ \quad + T_{366}^{\det 1} \cdot \delta^2 \\ Y^{\det 2} = T_{32}^{\det 2} \cdot \theta_0 + T_{33}^{\det 2} \cdot y_0 + T_{34}^{\det 2} \cdot \varphi_0 \\ \quad + T_{36}^{\det 2} \cdot \delta + T_{336}^{\det 2} \cdot y_0\delta + T_{346}^{\det 2} \cdot \varphi_0\delta \\ \quad + T_{366}^{\det 2} \cdot \delta^2 \end{array} \right.$$

It contains 26 transport coefficients, obtained from beam transport calculations and 4 measured positions $X^{\det 1}$, $Y^{\det 1}$, $X^{\det 2}$ and $Y^{\det 2}$ on the two detectors for each individual pion. The parameters relating the horizontal abscissa $X^{\det 1}$ and $X^{\det 2}$ (in cm) measured on the two detectors are given in table 2.1.

The parameters relating the vertical abscissa $Y^{\det 1}$ and $Y^{\det 2}$ (in cm) measured on the two detectors are given in table 2.2

The left over terms $T_{11}x_0$ and $T_{116}x_0\delta$ will give rise to the dominant contribution to the momentum resolution, the other contributions resulting from multiple scattering in the detector 1 and from the resolution on the measured positions $X^{\det 1}$, $X^{\det 2}$, $Y^{\det 1}$ and $Y^{\det 2}$ on the two detectors.

To solve this set of equation, we neglect in the first iteration the terms $T_{14}\varphi_0$ and $T_{146}\varphi_0\delta$ that couple to the vertical variables. Consequently, the first 2 equations of the set contains only the two variables θ_0 and δ and can then be solved independently. Expressing θ_0

Table 2.2: Numerical values of the transport coefficients in the vertical plane at the two detector positions.

Coefficient	Detector 1	Detector 2
T_{32}^{det} [cm/mrad]	-1.345×10^{-1}	-7.092×10^{-1}
T_{33}^{det} [cm/cm]	-1.860×10^1	-6.987×10^1
T_{34}^{det} [cm/mrad]	-3.839×10^{-3}	-8.523×10^{-1}
T_{36}^{det} [cm/%]	4.058×10^{-2}	1.468
T_{36}^{det} [cm/cm/%]	2.200×10^{-2}	9.286×10^{-2}
T_{346}^{det} [cm/mrad/%]	2.678×10^{-1}	9.965×10^{-1}
T_{366}^{det} [cm/% ²]	-3.777×10^{-3}	-1.638×10^{-1}

as a function of δ , this leads to the system:

$$\begin{cases} \theta_0 = \frac{X_{12}^{\det 1} - T_{16}^{\det 1} \cdot \delta - T_{166}^{\det 1} \cdot \delta^2}{T_{12}^{\det 1} + T_{126}^{\det 1} \cdot \delta} \\ \theta_0 = \frac{X_{12}^{\det 2} - T_{16}^{\det 2} \cdot \delta - T_{166}^{\det 2} \cdot \delta^2}{T_{12}^{\det 2} + T_{126}^{\det 2} \cdot \delta} \end{cases}$$

A third order equation in δ is then derived that reads

$$a_0 + a_1\delta + a_2\delta^2 + a_3\delta^3 = 0$$

with

$$\begin{aligned} a_0 &= X_{12}^{\det 2} T_{12}^{\det 1} - X_{12}^{\det 1} T_{12}^{\det 2} \\ a_1 &= \left(X_{126}^{\det 2} T_{126}^{\det 1} - T_{126}^{\det 1} T_{16}^{\det 2} \right) \\ &\quad - \left(X_{126}^{\det 1} T_{126}^{\det 2} - T_{126}^{\det 2} T_{16}^{\det 1} \right) \\ a_2 &= \left(T_{16}^{\det 1} T_{126}^{\det 2} + T_{12}^{\det 2} T_{166}^{\det 1} \right) \\ &\quad - \left(T_{16}^{\det 2} T_{126}^{\det 1} + T_{12}^{\det 1} T_{166}^{\det 2} \right) \\ a_3 &= T_{126}^{\det 2} T_{166}^{\det 1} - T_{126}^{\det 1} T_{166}^{\det 2} \end{aligned}$$

and is solved either formally or numerically with a starting value at $\delta = 6\%$. The θ_0 value can then be deduced. The values of θ_0 and δ are introduced in the last two equations, leading to the following linear system:

$$\begin{cases} \alpha y_0 + \beta \varphi_0 = \gamma \\ \alpha' y_0 + \beta' \varphi_0 = \gamma' \end{cases}$$

with

$$\begin{aligned} \alpha &= T_{33}^{\det 1} + T_{336}^{\det 1} \cdot \delta \\ \alpha' &= T_{33}^{\det 2} + T_{336}^{\det 2} \cdot \delta \\ \beta &= T_{34}^{\det 1} + T_{346}^{\det 1} \cdot \delta \\ \beta' &= T_{34}^{\det 2} + T_{346}^{\det 2} \cdot \delta \\ \gamma &= Y^{\det 1} - T_{32}^{\det 1} \cdot \theta_0 - T_{36}^{\det 1} \cdot \delta - T_{366}^{\det 1} \cdot \delta^2 \\ \gamma' &= Y^{\det 2} - T_{32}^{\det 2} \cdot \theta_0 - T_{36}^{\det 2} \cdot \delta - T_{366}^{\det 2} \cdot \delta^2 \end{aligned}$$

The solutions of this system are fed into the first 2 equations (the ones involving $X^{\det 1}$ and $X^{\det 2}$) which is solved again for providing the final values for θ_0 and δ . The convergence is quite fast and one iteration is enough to keep residuals on δ much below the per mil level. A second iteration on the second set of equations (the ones involving $Y^{\det 1}$ and $Y^{\det 2}$), thus provides final values for φ_0 and y_0 .

The relevant quantities for kinematical reconstruction of the events, p_x , p_y and p_z at the HADES target are derived from the values of θ_0 , φ_0 and δ through the formulae:

$$\begin{aligned} p &= p_{spec}(1 + \delta) \\ p_x &= \frac{p \tan(\theta_H)}{\sqrt{1 + \tan^2(\theta_H) + \tan^2(\varphi_H)}} \\ p_y &= \frac{p \tan(\varphi_H)}{\sqrt{1 + \tan^2(\theta_H) + \tan^2(\varphi_H)}} \\ p_z &= \frac{p}{\sqrt{1 + \tan^2(\theta_H) + \tan^2(\varphi_H)}} \end{aligned}$$

where θ_H and φ_H are obtained through the following relations (see table 2.3 for the coefficients)

$$\begin{aligned} \theta_H &= T_{22}^H \cdot \theta_0 + T_{23}^H \cdot y_0 + T_{26}^H \cdot \delta \\ &\quad + T_{226}^H \cdot \theta_0 \delta + T_{246}^H \cdot \varphi_0 \delta + T_{266}^H \cdot \delta^2 \\ \varphi_H &= T_{42}^H \cdot \theta_0 + T_{43}^H \cdot y_0 + T_{44}^H \cdot \varphi_0 + T_{46}^H \cdot \delta \\ &\quad + T_{426}^H \cdot \theta_0 \delta + T_{436}^H \cdot y_0 \delta + T_{446}^H \cdot \varphi_0 \delta + T_{466}^H \cdot \delta^2 \end{aligned}$$

Table 2.3: Numerical values of the transport coefficients between the pion production target and the HADES target.

Coefficient	Value
T_{22}^H [mrad/mrad]	-5.003 01
T_{23}^H [mrad/cm]	5.752×10^{-1}
T_{26}^H [mrad/%]	9.147×10^{-2}
T_{226}^H [mrad/mrad/%]	-8.205×10^{-2}
T_{246}^H [mrad/mrad/%]	3.102×10^{-3}
T_{266}^H [mrad/% ²]	2.538×10^{-2}
T_{42}^H [mrad/mrad]	3.481×10^{-2}
T_{43}^H [mrad/cm]	3.4273×10^2
T_{44}^H [mrad/mrad]	4.1839×10^{-1}
T_{46}^H [mrad/%]	-7.1969×10^{-1}
T_{426}^H [mrad/mrad/%]	-3.212×10^{-3}
T_{436}^H [mrad/cm/%]	-9.978
T_{446}^H [mrad/mrad/%]	-4.957×10^{-1}
T_{466}^H [mrad/% ²]	1.920×10^{-1}

Chapter 3

Silicon Detector

3.1 Silicon Sensors

The two silicon sensors, that are used for the CERBEROS system, consist of $10 \times 10 \text{ cm}^2$ n^+p doped silicon areas with a thickness of $300 \mu\text{m}$ (fig. 3.1). In order to guarantee a sufficient position resolution and to reduce the capacitive noise, the n^+ and the p sides are each segmented into 128 channels. As the segmentation is in horizontal direction on one side and in vertical direction on the other side, a combined x-y position information can be obtained.

3.1.1 Energy Resolution

In a first test the energy resolution and the signal to noise separation achievable with these silicon detectors have been tested in the laboratory with radioactive

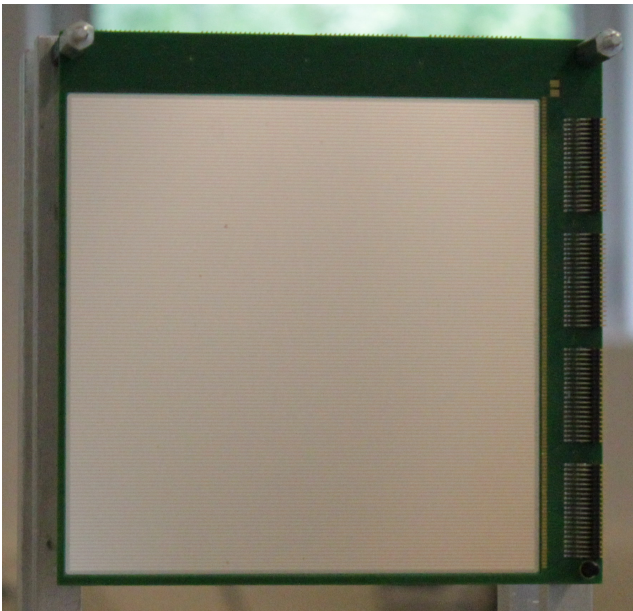


Figure 3.1: Photo of the silicon sensor. The sensor is glued to the base PCB, and its strips are bonded to corresponding pads on the PCB. The pads are connected to the SAMTEC connectors with copper routes. One row of connector for 128 channels is seen on the right side of the PCB. Other 128 connections are placed on the other side of the PCB on its top.

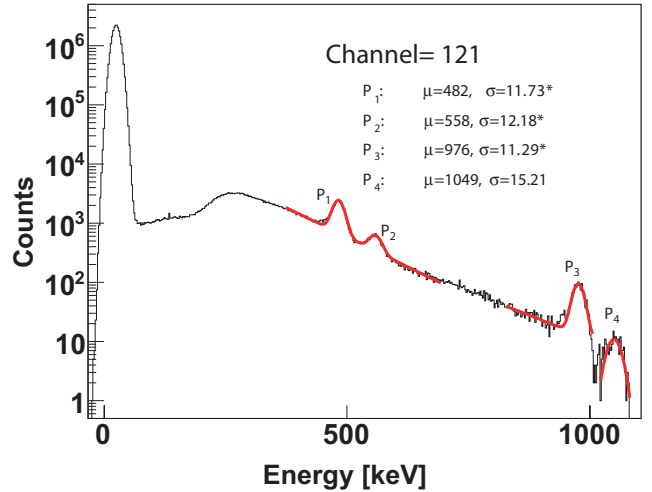


Figure 3.2: Energy spectrum of channel 121, measured with a ^{207}Bi source. The red lines show fits of exponential plus Gaussian functions. The legends indicate the fit results.

sources, using a Mesytec readout system. A ^{207}Bi β -source was used for the calibration. Figure 3.2 shows the calibrated energy spectrum for one of the altogether 256 channels.

The four dominant electron lines (482 keV, 554 keV, 976 keV and 1045 keV of ^{207}Bi are clearly associated to the four peaks in the spectrum which are used to calibrate the ADC values. In the calibrated spectrum the noise peak can then be fitted with a Gaussian. The

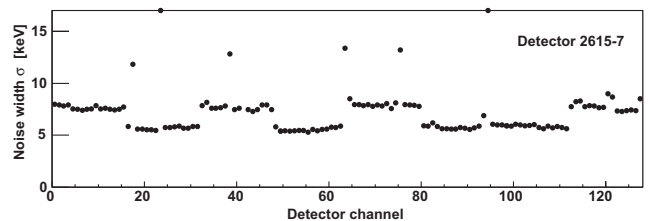


Figure 3.3: Calibrated noise width as a function of the channel number for one of the three tested detectors. The step like structures are attributed to the readout system and not to the detector itself. See text for details.

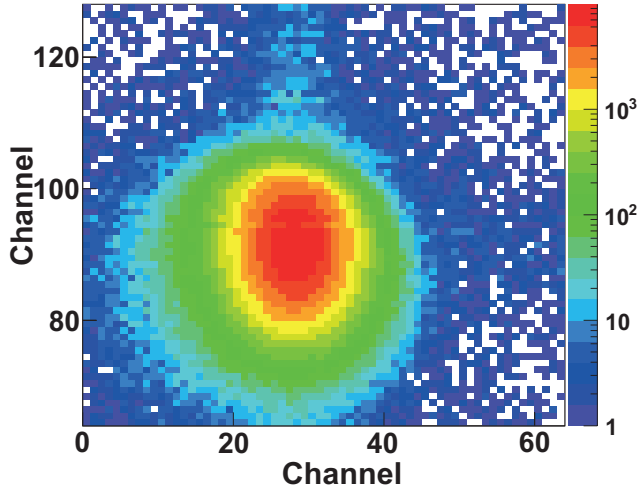


Figure 3.4: Hit pattern in one silicon detector. A scintillator served as an external trigger. The signals are induced by the β decay of a Sr source.

width of this Gaussian corresponds to the noise width in units of keV. By carrying out this calibration procedure for all channels independently, a noise-width pattern as a function of the channel number is obtained. It is presented for one of the three tested detectors in fig. 3.3.

For this measurement two neighbouring channels were connected together, resulting in only 128 individual points. The first 64 channels correspond here to the p side of the detector, whereas the remaining channels correspond to the n^+ side. The step like structures in the measure noise-width pattern result from the fact that two different kinds of preamplifiers have been used for the measurement. The channels with larger noise have been read out with logarithmic preamplifiers, the channels with lower noise with linear pre-amplifiers. The observed difference is consistent with the setup documentation, claiming a difference of about 30 % [15].

Using the low noise channels as a benchmark, a noise-width of $\sigma \approx 6$ keV has been determined. Comparing this to the signal position of ≈ 120 keV, induced by MIP particles in $300 \mu\text{m}$ silicon, a signal to noise separation of $120/6 = 20$ can be achieved.

The two other tested detectors show a similar good energy resolution.

3.1.2 Detector Efficiency

The second test concerns the efficiency of the silicon detectors. It was determined by placing the detector in between a Sr β -source and a scintillator. The scintillator was used as an external trigger, counting the electrons that pass the silicon and hit the scintillator. Figure 3.4 displays the obtained hit pattern for one of the three detectors after the noise suppression.

By integrating this spectrum and normalizing it to

Table 3.1: Efficiencies of the three different silicon detectors.

Detector	Efficiency
2615-7	97 %
2814-24	96 %
2814-25	92 %

the number of hits in the scintillator, the efficiency of each detector has been determined. The results are given in table 3.1. They are in agreement with the expectations for silicon detectors.

The third test of the detector concerns its radiation hardness. Indeed, it was claimed by the manufactures that the n^+p detectors are especially radiation hard. This statement was tested by impinging a high flux of 15 MeV protons from the tandem accelerator at MLL [16] on one of the detectors. The radiation induced damages are then determined from the increase in the measured leakage current via:

$$\Delta I = V\alpha\Phi_{eq} = d\alpha N_{eq} \quad (3.1)$$

where V is the irradiated volume, Φ_{eq} is the equivalent particle flux and α is a parameter, which characterizes the sensitivity of the detector to radiation damages. Cancelling out the irradiated area, the formula can also be expressed by the detector thickness d and the number of hitting particles N_{eq} . Indeed, for the quantification of the radiation hardness the factor α is normally used as a reference parameter.

In order to allow later on a comparison with other experiments the measured particle flux Φ ($[\frac{1}{\text{cm}^2}]$) is normalized to an equivalent flux Φ_{eq} of neutrons with 1 MeV kinetic energy. The damages, induced by a particle flux Φ , is then the same as if 1 MeV neutrons with a flux of Φ_{eq} would have been used instead. Figure 3.5 shows the measured current increase ΔI as a function of the exposed particle dose N_{eq} .

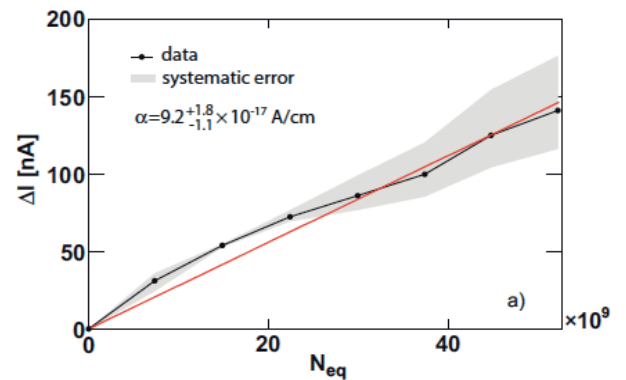


Figure 3.5: Measured increase in the leakage current as a function of the equivalent particle dose N_{eq} .

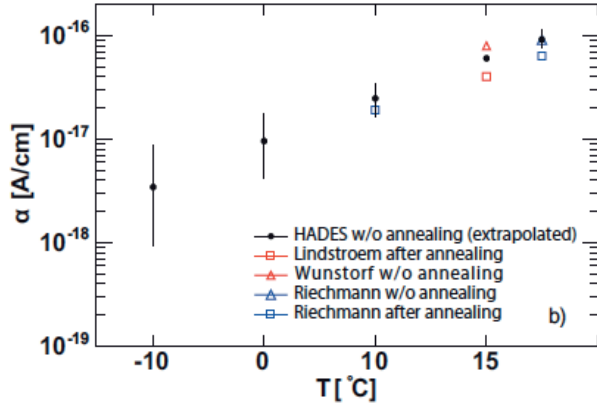


Figure 3.6: α from equation (3.1) for different temperatures and different experiments [16–18].

The linear behaviour of the data points can be fitted with eq. (3.1), leading to an α value at a temperature of $T = 25^\circ\text{C}$ of $\alpha_{25^\circ\text{C}} = 9.2_{-1.1}^{+1.8} \times 10^{-17} \text{ A cm}^{-1}$. In fact, the extracted value of α depends strongly on the temperature, which can easily be understood from the temperature dependence of the leakage current itself. Furthermore, α shows a strong dependence on the time after the radiation period. If the detector has time to anneal, the amount of damages in the detector reduces and so does α . In our measurement, however, the detector properties are measured without annealing. In fig. 3.6 we show our extracted value for α , normalized to different temperatures, and compare this to other measurements of silicon detector radiation hardness, reported in the literature. An important observation is that the measurements with a certain annealing time show always lower values of α , whereas the measurements without annealing are in very good agreement with our results. This indicates that the n^+p detectors, which will be used for the pion beam time, show the same radiation hardness as any normal p^+n doped silicon detector.

Next one can investigate the amount of radiation both detectors are exposed to as well as the thereby provoked increase in the leakage current over the whole pion beam time of 4 weeks. At the first detector an intensity of $N_{\pi,1} = 1 \times 10^7 \pi \text{ s}^{-1}$ is expected and at the second one an intensity of $N_{\pi,2} = 1 \times 10^6 \pi \text{ s}^{-1}$. Those intensities and the ratio of irradiation damage κ for pions at an energy of 1 GeV with an value of $\kappa = 0.55$ (see fig. 3.7) yield to the following exposed particle doses: $N_{eq,1} = 1.3 \times 10^{13}$ and $N_{eq,2} = 1.3 \times 10^{12}$. Using eq. (3.1) and the extracted damage rate α value of $\alpha_{25^\circ\text{C}} = 9.2 \times 10^{-17} \text{ A cm}^{-1}$, the increase in the leakage current at the end of the pion beam time can be determined. Hence the leakage current is increased by $\Delta I_1 = 37 \mu\text{A}$ for the first and by $\Delta I_2 = 3.7 \mu\text{A}$ for the second detector. The increase for the first detector can be even higher due to the bulk damage caused by

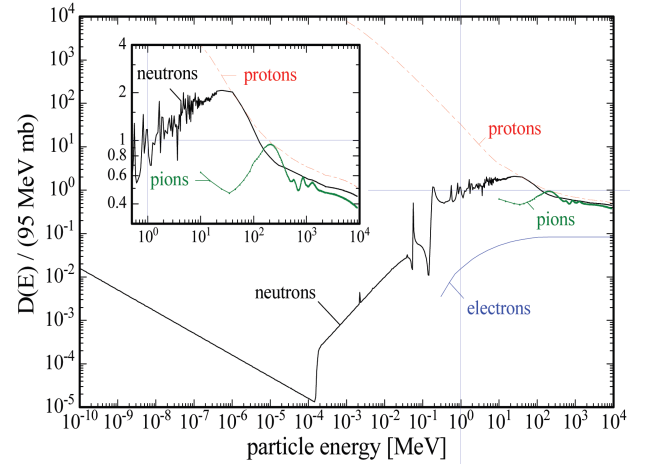


Figure 3.7: Displacement damage cross section as a function of energy for different particles normalized to neutrons at 1 MeV[17].

traversing neutrons.

3.2 Energy deposition in thin detector layers

In a thin layer, corrections to the standard Bethe-Bloch formula for energy loss are needed to deduce the corresponding energy deposition and the so-called restricted formula has to be used. Indeed, the δ -electrons can be knocked-out from the detector active surface leading to a deposited energy smaller than the energy loss. As a result, the pion momentum leading to the minimum energy deposition in a $300 \mu\text{m}$ Si layer is $750 \text{ MeV}/c$ instead of $450 \text{ MeV}/c$, where it coincides with the Minimum Ionizing momentum, as shown in fig. 3.8[19]. Additionally the relativistic rise of the energy deposition above the MIP region is flatter for the case of the thin layer (fig. 3.8a). This effect has been measured and confirmed by a dedicated experiment at BNL by HEPHY and MIT – fig. 3.8b[19].

3.2.1 Impact on the Pion Tracker performance

With expected momenta value in range of $1 \text{ MeV}/c$ to $2 \text{ MeV}/c$, the minimum ionizing pions will deposit only around 80 MeV in the silicon. The open questions are therefore the separation (or Signal-to-Noise Ration, SNR) between energy peak and noise and optimal threshold settings. Details and discussion about SNR calculations and threshold optimisations are in section 7.1.

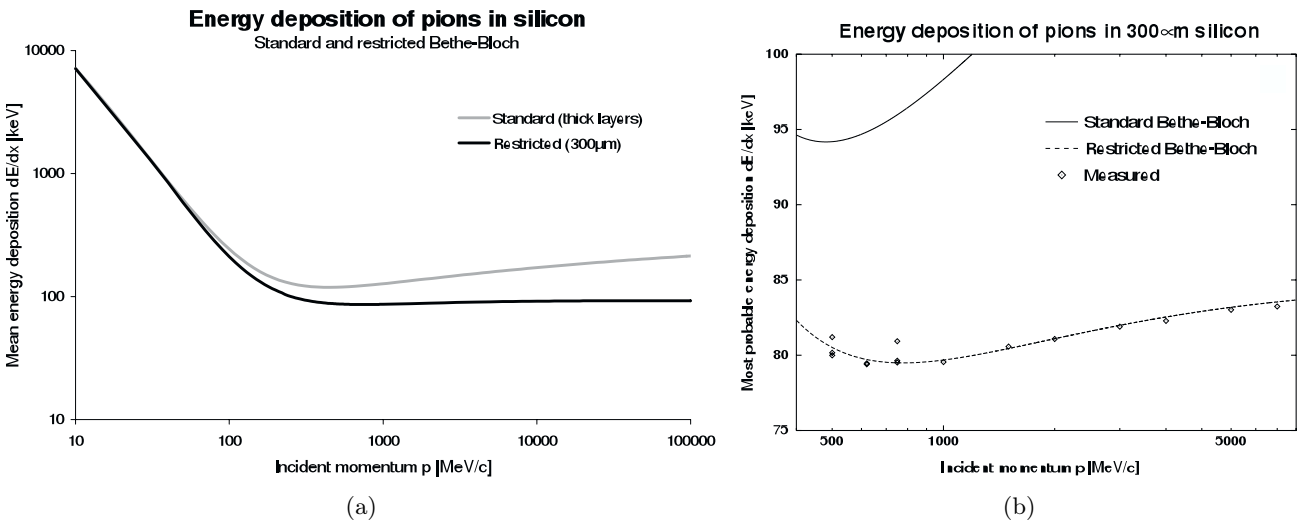


Figure 3.8: Energy deposition of pions in silicon: (a) theoretical and (b) measured.[19]

Chapter 4

Detector Cooling

4.1 Thermal simulation

Since the silicon device is located in vacuum it becomes mandatory to cool the system.

The planned cooling device for the silicon system consists of two quadratic FR4 blocks ($l = 139$ mm, $d_{top} = 5.5$ mm, $d_{bottom} = 3$ mm), which surround the detector. Mounted on each block there are two bent copper plates ($l_{1,top} = 12$ mm, $l_2 = 95$ mm). The copper plates are connected to the silicon wafer through heat conduction pads that are included as a thermal resistance ($\lambda = 2$ W mK⁻¹, $d = 0.5$ mm) into the simulation so that the copper plates directly transfer the heat to the wafer. These heat conduction pads isolate voltages up to 10 kV and ensure that the copper plates introduce no short cuts on the silicon wafer. The copper plates are located parallel to the strips of the wafer. The mechanical drawing of the cooling block is shown in fig. 4.1. This type of construction may cause that parts of the active area becomes inactive and thus some read-out channels are unusable. To minimize this loss, the contact area ($l_{contact-area} = 3.5$ mm) is kept as small as possible. Every copper panel introduces a loss of about 5 mm of the active area, leading to

about 7 inactive stripes ($N_{channel} = 5$ mm/ $d_{pitch} = 5$ mm/ 0.775 mm ≈ 6.5).

Overall 28 read-out channels become unusable. This assembling minimizes the temperature gradient, because the contact area of the two copper plates on the top is perpendicular to the area of the plates at the bottom of the detector. Therefore the wafer is cooled from all four sides. The copper plates are 0.1 mm thin that they do not apply to much pressure on the wafer.

The silicon detector is located in a vacuum pipe. The outer side of the vacuum pipe is set to 20 °C and Propan is used as cooling liquid at a temperature of -15 °C. The glue between the silicon wafer and the PCB is included in the simulation as a thermal resistance ($\lambda = 0.18$ W mK⁻¹, $d = 0.1$ mm). Moreover heat is exchanged through heat radiation between the elements. The simulation is based on the Finite Element calculation.

Figure 4.2 shows a quite homogeneous temperature distribution on the detector due to the cooling from all four sides. The temperature of the silicon wafer is around -10 °C as one can see from the temperature scale. The influence of the detector bias (100 V) and leakage current (2 μ A) on heat generation was exam-

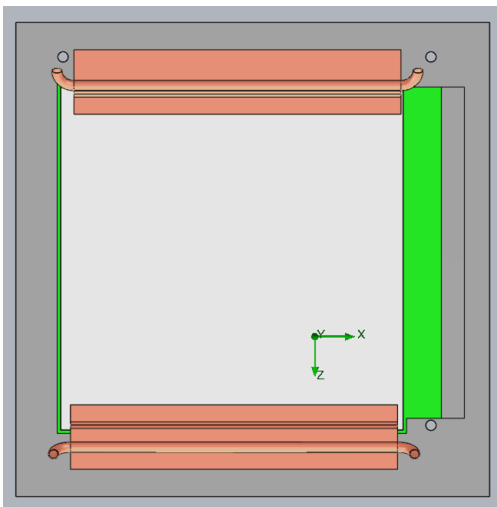


Figure 4.1: Mechanical drawing of the cooling block on the detector.

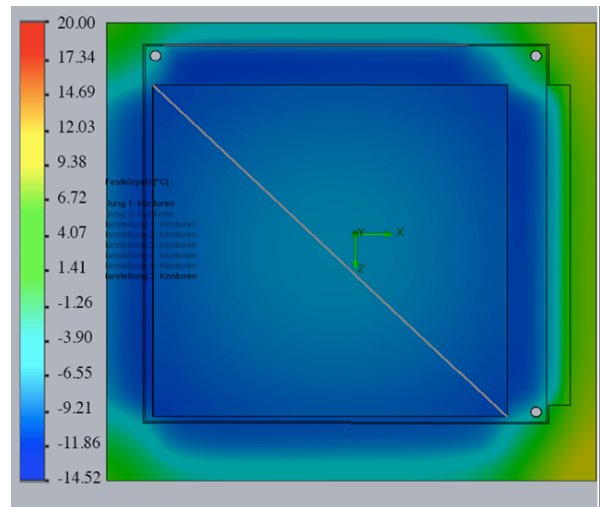


Figure 4.2: Simulated distribution of the temperature for cooled detector.

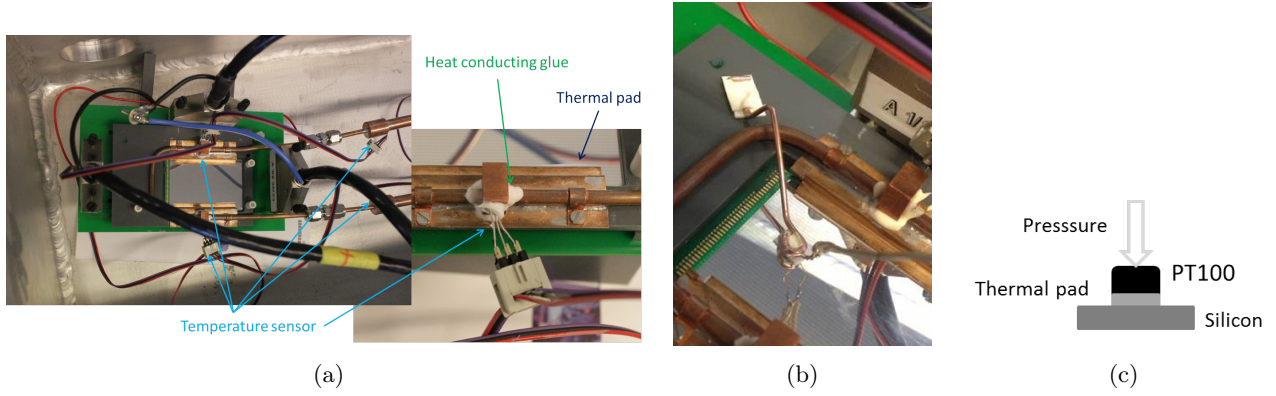


Figure 4.3: Prototype of the cooling device on the testing detector. It is placed in the vacuum chamber, several sensors located around the device (a) allows the temperature control. The Pt100 sensor (b) is slightly pressed on the silicon surface (c).

ined, too. It turned out that this heat source does not affect the temperature. All in all there are only little losses, so the cooling device works fine.

4.2 Experimental Setup

The test setup (fig. 4.3a) consists of a test-detector, which is located in a vacuum chamber with pressures down to 10^{-3} mbar. 1-wire temperature sensors (DS1820) are used for the temperature measurement. The sensors are attached to the cooling pipes via heat conducting glue to guarantee a good heat contact. The detector is cooled with a cooling bath thermostat MPC-K6s from Huber that uses a water-propylenglycol mixture as cooling fluid.

Temperatures down to -10°C were reached while the temperature of the fluid in the cooling bath thermostat was around -15°C . There is always a difference between those two temperatures due to thermal losses, which increases with lower temperatures. But this can be enhanced by an optimized isolation of cooling tubes. For the temperature measurement of the silicon a Pt100 sensor, which was slightly pressed on the silicon surface

(figs. 4.3b and 4.3c) to ensure a tolerable heat contact, was used.

In fig. 4.4a the silicon temperature is plotted as a function of the cooling fluid temperature. One can see that the difference grows with decreasing temperatures and that silicon temperatures down to $\approx -4^\circ\text{C}$ were reached.

One of the main aims of the test was to verify that the leakage current and the noise of the detector decreases because of cooling. So far it can be confirmed that the leakage current gets lower (fig. 4.4b), but does not show the theoretical behaviour:

$$I(T) \sim T^2 e^{-\frac{E_g}{2k_B T}} \quad (4.1)$$

where E_g is the band-gap energy (1.12 eV). At a cooling fluid temperature of -15°C equivalent to a silicon temperature of about -4°C (see fig. 4.4b). The leakage current should be 12 % of $I(20^\circ\text{C})$, which is $0.29 \mu\text{A}$, and not around $1.6 \mu\text{A}$.

Having now a look on the ramping curve in fig. 4.4c one can see that the leakage current has not the diode like behaviour, which can be a reason why the leakage current has also not the theoretical temperature dependence.

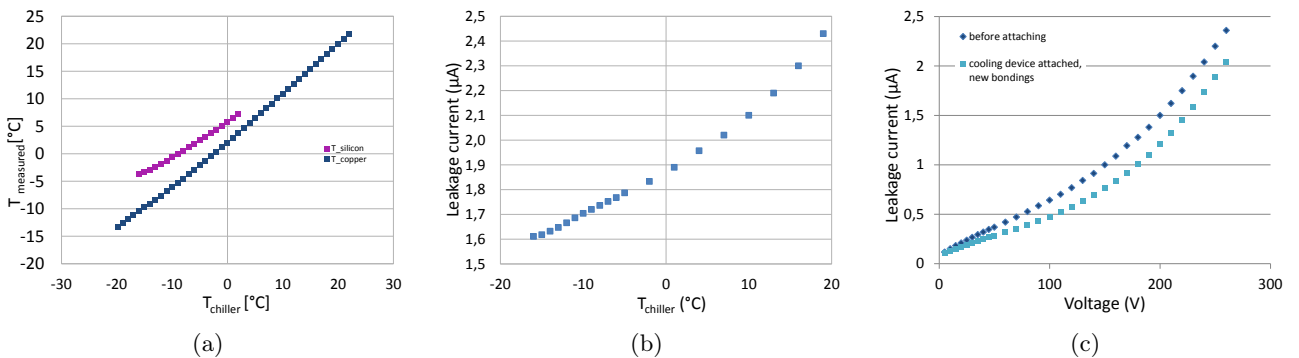


Figure 4.4: (a) Temperature in the different measuring points as a function of the cooling fluid temperature in the cooling bath thermostat. (b) Leakage current as a function of the cooling fluid temperature. The cooling induces a reduction of the leakage current. (c) Leakage current as a function of the applied voltage.

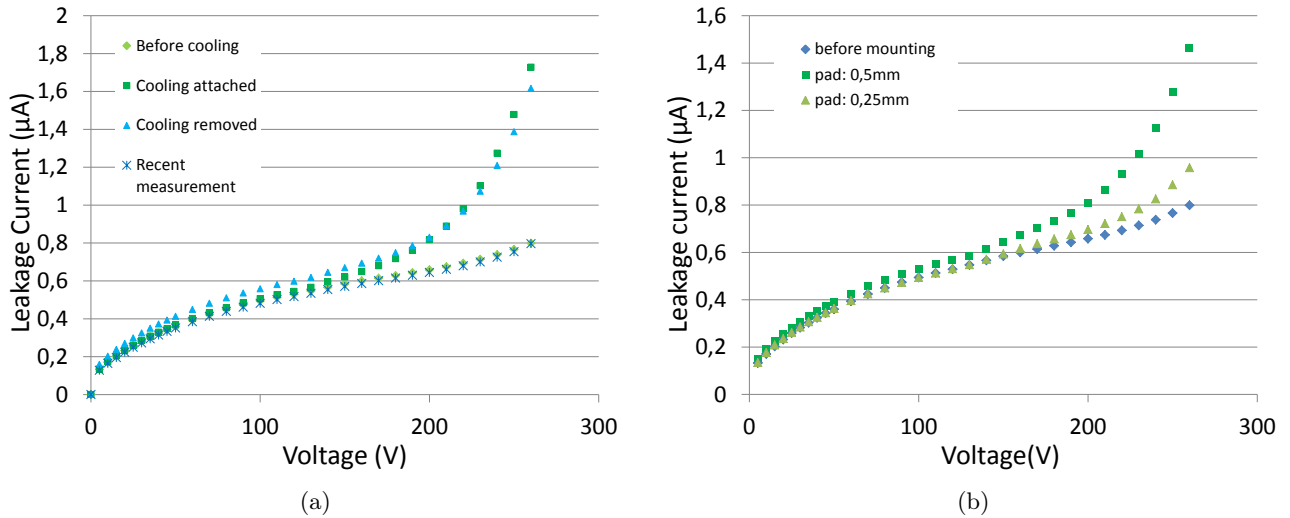


Figure 4.5: (a) Ramping curves measured during cooling tests. After attaching the cooling device, characteristic of the leakage current changed and stayed the same after removing cooling. New measurement after a few days showed characteristic the same like before first cooling attaching. (b) Comparison of different ramping curves for different thermal pad thickness (Thermal pad: 0.25 mm (Keratherm 86/82) and 0.5 mm (Keratherm–Softtherm 86/300)) with the one before the cooling device was mounted.

As a next step the detector was exchanged with the one, which has a normal diode like behaviour. In addition the swapped detector has the theoretical temperature dependence behaviour, which was proved during a “day-and-night measurement”. Therefore the detector was located in a light tight box, where the air was constantly exchanged and one can assume that the detector has the same temperature as the environment. By turning on the air condition we were able to change the temperature. Then we compared the leakage current with the temperature measured by a sensor near the detector.

Afterwards the cooling device was mounted on the new detector and for the first time a change in the

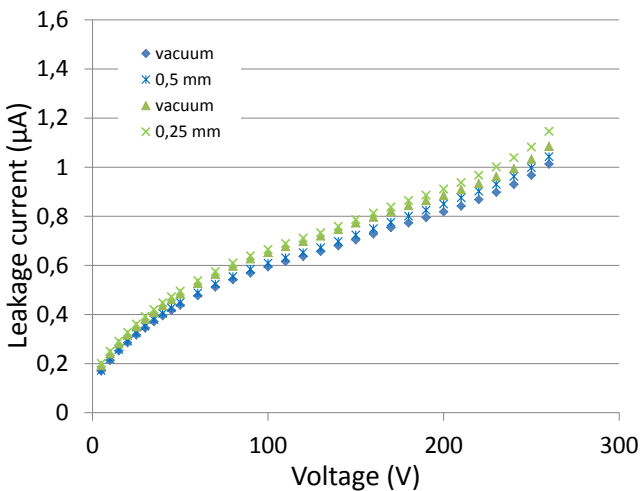


Figure 4.6: Investigation of the leakage current behaviour influenced by attaching the thermal pads on the detector.

leakage current behaviour, due to the attaching of the cooling device, was visible (fig. 4.5a dark green dots).

The cooling system introduces a break down behaviour of the detector before the depletion voltage is reached. Short after the whole cooling device was removed, the behaviour of the leakage current stayed the same. After some days the leakage current behaved normal again.

As a next step we exchanged the thermal pads to detect if the thermal pads are responsible for the modified leakage current behaviour.

Looking at fig. 4.5b one can see that the break down of the detector starts at a higher voltage for a thinner thermal pad. In more detail the break down begin now at around 240 V and not at 150 V like before, if the cooling device was attached. The bended copper plates seems to offer too much mechanical stress on the surface of the detector and introduce therefore the break down behaviour in leakage current, since the distance of the bended copper plates to the surface is fixed. This assumption can be confirmed by looking at the behaviour of the leakage current, if only the thermal pads are attached to the surface of the detector (fig. 4.6). One can see a little increase of the leakage current, but this can also be due to thermal fluctuation.

4.2.1 Conclusion and Outlook

Since the mechanical pressure is responsible for the behaviour, its planned a new setup (fig. 4.7) were the pressure on the surface can be controlled. But then it needs to be checked if the heat contact is still sufficient. Therefore the temperature measurement needs to be redone. Moreover we have to measure how does

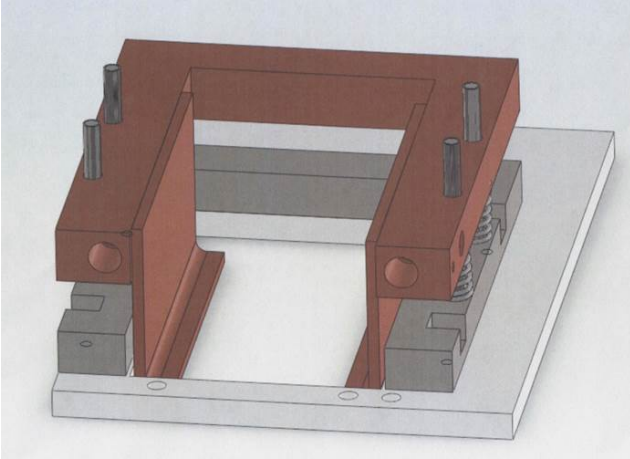


Figure 4.7: New cooling device prototype where the pressure on the silicon surface can be controlled via springs.

the energy resolution change during cooling. The leakage current for different temperatures needs to be measured and checked if it is consistent with the theoretical curve. If the leakage current behaviour can not be under control, the different concept of the *indirect cooling system* must be considered.

4.3 Indirect cooling

A passive cooling implies that no parts other than the PCB touch the silicon wafer (see fig. 4.8 left). This should eliminate the danger of a rise in the leakage current, caused solely by mounting the cooling system.

The problematic point of the passive cooling is the low heat conductivity of the PCB made of FR4 of around $\lambda = 0.3 \text{ W mK}^{-1}$. Due to the non-trivial geometry of the PCB the heat conductivity can't be easily calculated. Therefore a finite element simulation was done with Solid Works. The simulation included only heat conduction, a constant outside temperature and a volume-heat source in the silicon. From the simulated temperature gradient between silicon and outside dependent on the volume-heat source we could estimate the heat conductance of the PCB to $50(10) \text{ mW K}^{-1}$. This value includes the glue between silicon and PCB as well as slightly varying mounting conditions of the PCB to the surrounding cooling parts.

The heat conductivity of the active cooling (see setup in section "Direct cooling": copper foil and heat conducting, isolating pad) can be calculated due to the much simpler geometry. The result for the current prototype version is a heat conductance of about 200 mW K^{-1} , which is mainly limited due to the thin foil ($d = 0.1 \text{ mm}$) and limited heat conductivity of the pad ($\lambda = 1 \text{ W mK}^{-1}$). If necessary these values could be improved by a factor of 3 or 4.

A comparison of both approaches in terms of heat conductivity shows, that the active cooling is clearly superior if the problems of the rising leakage current

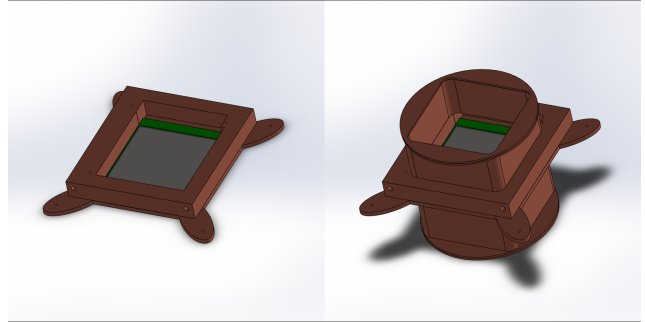


Figure 4.8: 3D-model of the cooling device without (left) and with (right) fridge.

can be solved. Nevertheless, since the problems are not solved jet, we thought about possible improvements of a passive cooling system.

The only way to significantly change the heat conductivity of the PCB is to use another material (e.g. a ceramic PCB), which in our case is problematic since the detectors are already purchased and an alternation of these would be necessary. Another way is to decrease the heating power that is supplied to the silicon. The main heating sources are heat radiation (some hundred mW) and thermal conduction through the readout cables (200 mW K^{-1} to 400 mW K^{-1}). The energy deposition of the particle flux and the leakage current are only minor effects (both $< 1 \text{ mW}$).

4.3.1 "Fridge"

The heat radiation could be reduced by mounting a cooled copper tube around the detector that shields the incoming heat radiation (20°C) from the chamber and vacuum pipe (see fig. 4.8 right). This fridge could cover $\approx 2/3$ of the solid angle seen from the silicon.

The effectiveness of a fridge was also simulated via a finite element simulation with Solid Works, tak-

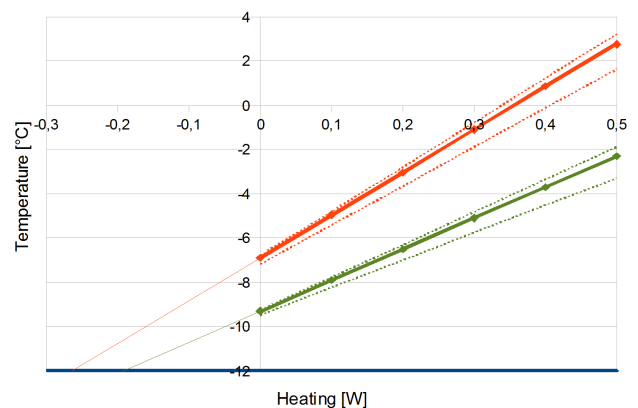


Figure 4.9: Orange curve: without fridge, green curve: with fridge. Curves show the average temperature of the silicon, dashed lines represent minimum and maximum temperature.

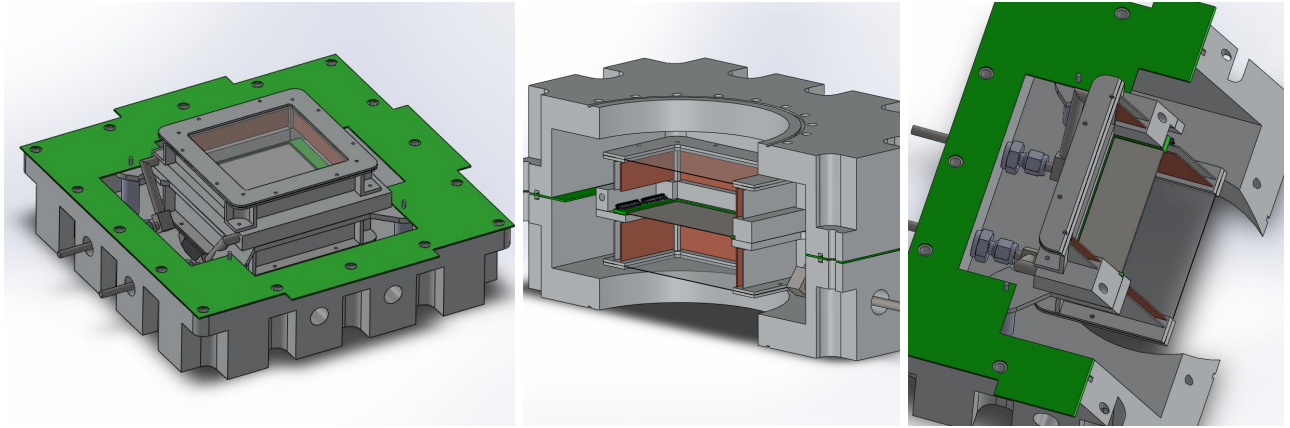


Figure 4.10: CAD drawing of the indirect cooling system inside the vacuum chamber. The left picture shows experimental vacuum chamber without upper closing, the fridge is placed inside. Middle and right picture shows cross-section of the chamber together with detector inside the fridge. See section 5.1 for details about vacuum chamber.

ing into account heat radiation and heat conduction. The boundary conditions were cooling liquid (water, -12°C), ambient radiation (black body radiation, $T = 20^{\circ}\text{C}$), copper-tube (emissivity inside $\epsilon = 0.57$ (oxidised), emissivity outside $\epsilon = 0.03$ (polished)) and silicon surface (emissivity $\epsilon = 0.04$ (polished aluminium)). In fig. 4.9 one can see that with varying heat source (0 W to 0.5 W) the fridge keeps the silicon 2.5°C to 4.5°C colder. Additionally one can see that a decrease in the heating of 100 mW results in a temperature decrease of 1.5°C .

A thin foil, that does not influence the beam particles, could be placed in the beam line near the silicon to reflect heat radiation.

The readout cables could be cooled by pressing them to the copper block that is also used for mounting the PCB and the other parts of the cooling. This would reduce heat flow from the front-end electronics to the detector by capturing heat by the significantly colder

cooling elements.

Figure 4.10 shows CAD drawing of the fridge inside the vacuum chamber.

4.3.2 Experimental setup

The experimental setup (fig. 4.11 left), that consists of the indirect cooling prototype and the mechanical sample of the pion tracker, is located inside a testing vacuum chamber (different that shown in fig. 4.10 and fig. 4.11 right) with pressures down to 10^{-3} mb. Four 1-wire temperature sensors were attached with a heat conducting glue (NEE 001/NEE 002) to the following places:

- into the plastic cooling tube shortly before the vacuum chamber entrance ("tube")
- to the copper cooling pipe before the detector cooling structure ("pipe in")

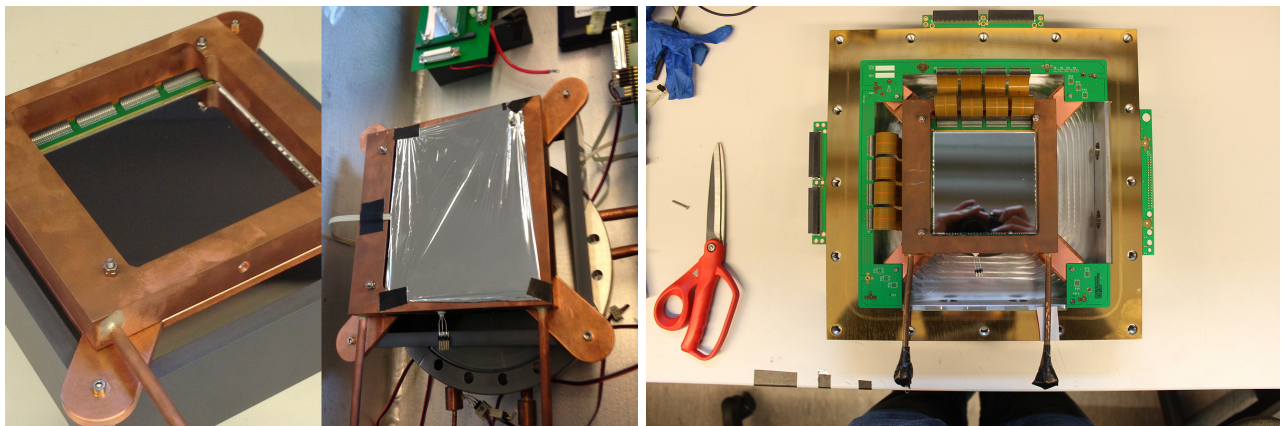


Figure 4.11: Pictures of the experimental setup. Left: The indirect cooling prototype with the mechanical sample of the pion tracker detector. Middle: Indirect cooling system in test vacuum chamber with reflecting Mylar foil (thickness $1.5\text{--}2\ \mu\text{m}$, weight $252\ \mu\text{g cm}^{-2}$). Right: Cooling system inside vacuum chamber (see section 5.1 for details about vacuum chamber).

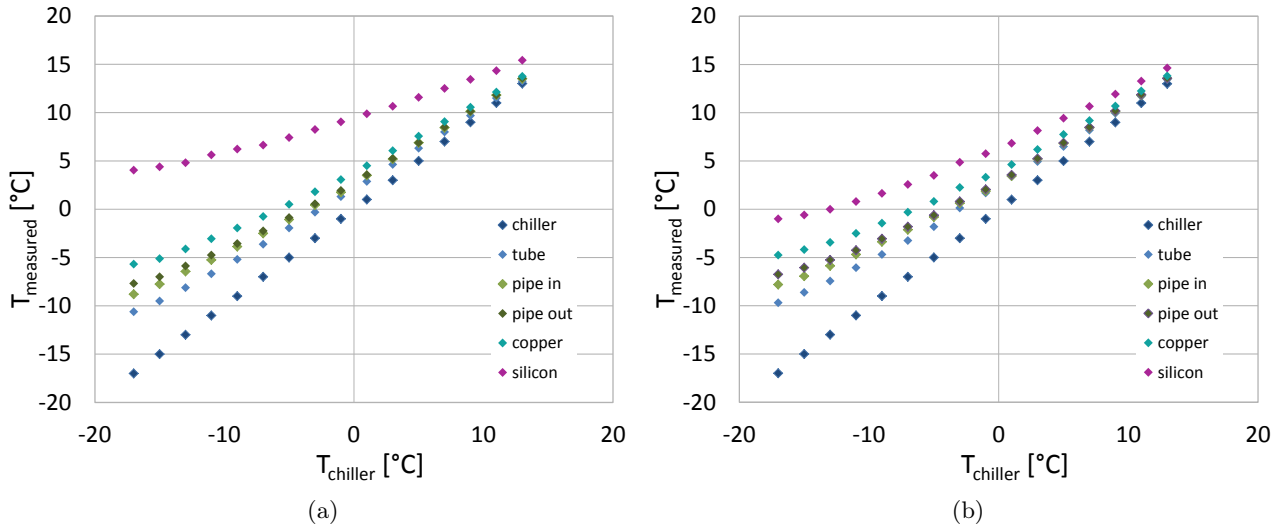


Figure 4.12: Temperatures measured by the different sensors as a function of the cooling fluid inside the chiller, before (a) and after (b) a Mylar foil was mounted in front of the silicon.

- to the copper cooling pipe after the detector cooling device ("pipe out")
- to the detector cooling block ("copper")

While the temperature of the detector is measured by a Pt100 temperature sensor, which is slightly pressed to the surface ("silicon").

With the indirect cooling system, silicon temperatures down to $\sim 4^\circ\text{C}$ are reached. One can see in fig. 4.12a that largest losses are between the copper and the silicon, due to the limited heat conduction of the PCB, as well as from the chiller to the vacuum chamber.

By remeasuring the temperature curves with a Mylar foil¹ mounted on both sides of the silicon (fig. 4.12 right) to shield the incoming heat radiation, silicon temperatures down to $\sim -1^\circ\text{C}$ are reached. Hence the

¹Area density $\rho_{A,2\text{ foils}} = 350\ \mu\text{g cm}^{-2} = 0.005\ \rho_{A,\text{silicon}}$, $\rho_{A,\text{silicon}} = 70\ \text{mg cm}^{-2}$.

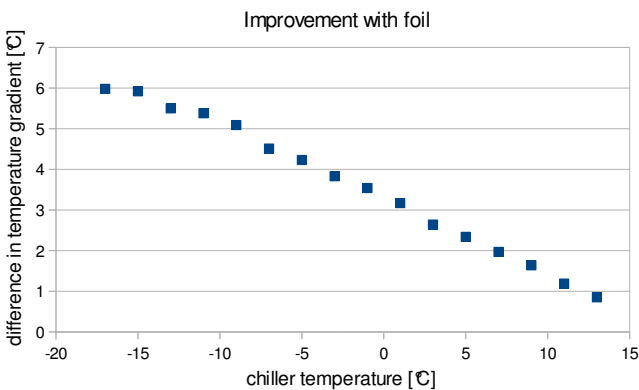


Figure 4.13: The reduction of the temperature difference between copper cooling block and silicon due to a Mylar foil, which reflects thermal radiation.

temperature gradient between the cooling fluid temperature inside the chiller and shortly before the vacuum chamber is dominant now. This gradient can be reduced by improving the thermal isolation of the tubes outside the vacuum chamber as well as increasing the liquid flow by enlarging the diameter of the pipes inside the vacuum chamber.

To further analyse the influence of the reflecting Mylar foil, one can compare the temperature gradient copper-silicon for the setup with and without the foil: $\Delta T_{\text{foil}} = \Delta T_{\text{copper-silicon,with foil}} - \Delta T_{\text{copper-silicon,without foil}}$. At a cooling fluid temperature inside the chiller of -17°C the temperature difference $\Delta T_{\text{foil}} \approx 6^\circ\text{C}$ (fig. 4.13). Hence the temperature gradient was reduced from 10°C to 4°C .

Schedule

The next step is the optimisation of the cooling liquid circuit, which should enable us to cool the silicon to the aimed temperature range. Moreover it needs to be investigated if the cooling system can provide a stable detector temperature over a longer timescale. Additionally the effect of the thermal stress caused by the different thermal expansion coefficients of silicon and PCB has to be estimated for the indirect cooling. This can be done by measuring the leakage current of the pion tracker detector over the whole temperature range of the chiller by decreasing the temperature step by step.

Chapter 5

Mechanical Structure

5.1 Vacuum Chamber

The CERBEROS detectors are mounted in two separated places along the beam-line between the pion production target and the HADES spectrometer. Thus each detector must be enclosed in a vacuum and light tight chamber, compatibly with the pipe mechanics. The single chamber is built of two identical aluminium blocks placed together face-to-face. One of the blocks has additional openings for the cooling. A view of one half of the chamber is shown on fig. 5.1. The technical drawing is on fig. 5.2.

Between the two halves of the chamber a feed-through PCB is placed (like in a sandwich). Vacuum tightness between the aluminium blocks and the PCB is provided by two o-rings placed in the grooves on the blocks. On the two sides of one block additional removable U-shaped frames are attached to be used as holder for the front-end electronics.

5.1.1 Feed-through boards

The PCB (fig. 5.3) placed between two blocks of aluminium provides electrical connections between the

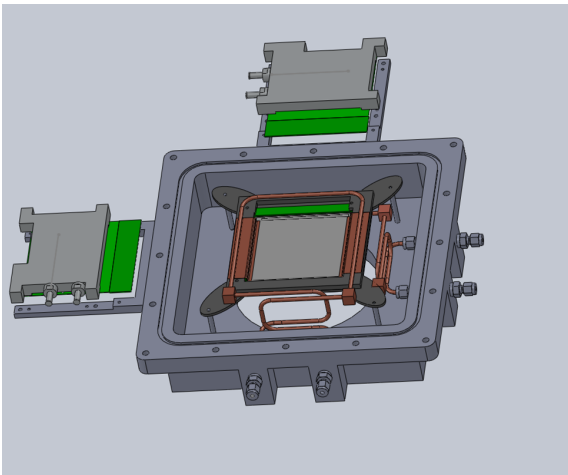


Figure 5.1: View of one half of the vacuum chamber. The detector together with the cooling is located in the central part of the chamber. The front-end modules are mounted on the two external sides of the chamber.

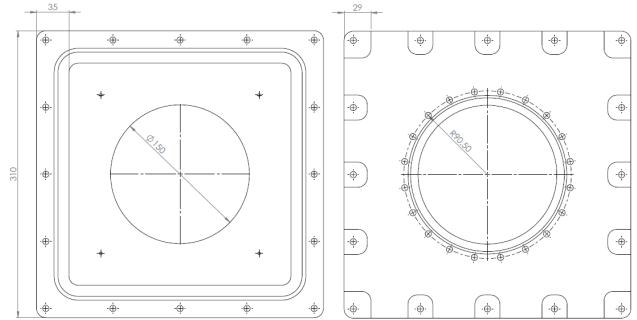


Figure 5.2: The inner part of the chamber on the left side and the other one on the right side.

chamber inside and outside. The two balconies visible on the left side and on the top of the board are

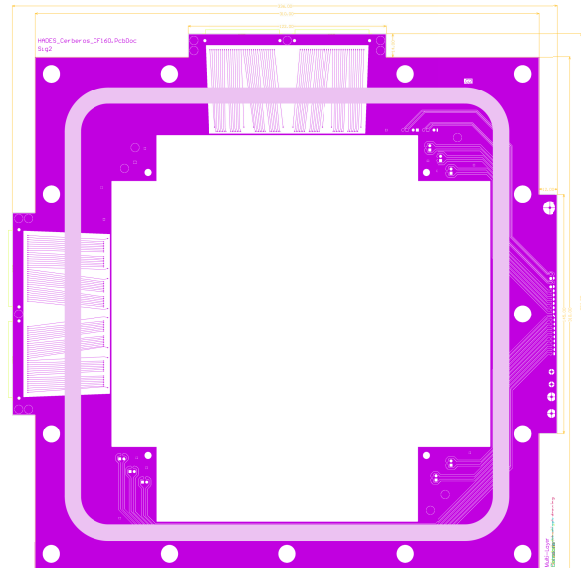


Figure 5.3: Layout of the inner layers of the feed-through PCB. The basic rectangular shape fits to the size of the chamber. The smaller bright rectangle with rounded corners depicts the place where the o-rings will touch the surface and this zone should be very flat to provide the best vacuum tightness.



Figure 5.4: Vacuum feed-through of plastic for the cooling.

equipped with ERNI connectors for connecting the detector signals to the front-end electronics. On the third edge the connector for temperature sensors and other helper connections (for maximum 16 LVDS pairs) is located. The inner cut-out in the PCB is made for detector mounting. The connection between the silicon detector and the PCB is made by Kapton tapes of length of 70 mm. Additional connectors on the corners of the cutout are for temperature sensors.

5.1.2 Vacuum feed-through for cooling

There are now two possibilities for the vacuum feed-through. One is with plastic screws (fig. 5.4) and the other one with a construction of stainless steel (fig. 5.5). The plastic one is screwed in and the metal feed-through is stucked through the chamber and tightened with a female screw. The vacuum tightness is given in both cases via an O-ring. For the plastic screw the O-ring is outside and for the metal one inside the chamber. The comparison between those two methods is shown in table table 5.1.

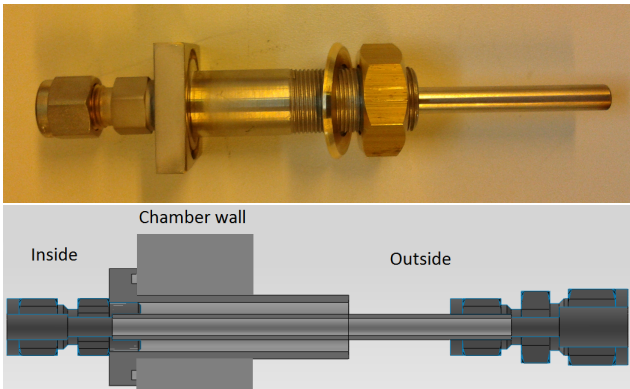


Figure 5.5: Vacuum feed-through of metal for the cooling. The left side is in the chamber and the pipe on the right side is connected to the cooling.

Table 5.1: Measurement of vacuum tightness for plastic and metal feed-throughs at different temperature of the cooling liquid.

temp.	plastic	metal
35 °C	7.8×10^{-8} mbar	not measured
20 °C	6.7×10^{-8} mbar	3.0×10^{-7} mbar
-5 °C	6.2×10^{-8} mbar	not measured
-15 °C	5.3×10^{-8} mbar	not measured

These are the results obtained up to now. For the metal one the tests just started, so the pressure might get lower. Also the measurements with cooling will be done.

5.2 Testing procedure

To verify whether this construction provides sufficient tightness for the vacuum, the PCB together with the chamber were tested in the laboratory. The PCB was placed between two pieces of the vacuum chamber. Both CF-160 openings (fig. 5.2 right) was closed with blind caps, tightness on the PCB side were provided by the o-rings in each part of the chamber.

Tests performed by Erwin Schwab and Technology Laboratory in GSI Darmstadt have shown the very good results, a leakage rate of 10^{-9} mbar l s⁻¹.

Further, the chamber will be tested together with detector cooling system in following steps:

1. Testing of vacuum tightness with closed inputs and dummy PCB between aluminium blocks.
2. Tightness tests of the cooling system inside the vacuum environment.
3. Tests of the cooling device within the testing (SiAVio) silicon detector.
4. Tests of the full system with Cerberos silicons.

5.3 Chamber mounting

While mounted on the beam line the centre of the chamber will be located on height of around 2m. One chamber will be placed in the NE5 Area (fig. 5.6a) and the other one in the HADES cave (fig. 5.6b) directly after the first quadropole. In NE5 there will be no additional holding structure for the chamber and in the HADES cave the chamber will be placed on some aluminium profiles as shown on figure fig. 5.7.



Figure 5.6: (a) Chamber position in the NE5 area. Chamber will be mounted directly before quadrupole. Beam comes from the right side. (b) Chamber position in the HADES cave. Beam comes from the wall direction.



Figure 5.7: The vacuum chamber mounted in the NE5 area.

Chapter 6

Front-End and Readout Electronics

6.1 The n-XYTER Readout

The n-XYTER[20] ASIC is a representative of a modern readout electronics systems for silicon detectors. It has 128 individual, self-triggered signal channels; a four words deep storage memory for data buffering and de-randomizing; and a synchronous mixed analogue-digital output (the analogue output delivers the energy information, whereas the digital delivers the time-stamp, the channel number and status information) for data streaming. It was designed for neutron experiments by the DETNI collaboration. The name n-XYTER itself stands for (*neutron*) *X*, *Y*, *Time and Energy Readout*. The n-XYTER works with positive and negative input charge polarities. The dynamic range of the input signal is 6 MIPS. Figure 6.1 shows the block diagram of the n-XYTER. It can be divided into five major parts (not all seen on the figure):

- front-end with two shaping routes,
- back-end with a token ring architecture,
- DAC (digital-analogue converters),
- time-stamp generator,
- slow control interface.

Each channel has an individual front-end block with two signal processing routes designed for positive and

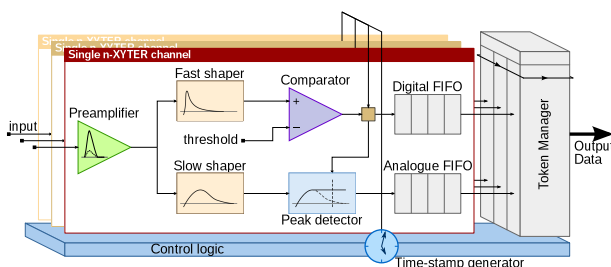


Figure 6.1: Block diagram of the n-XYTER architecture. The front end part is individual for each channel. The back-end part joins all channels (token ring architecture) and streams data to a single output bus. The DAC and time-stamp generator deliver common biasing and a time reference for all channels.

negative input charge polarities. The fast shaper is optimized for time measurement and has peaking time of 18.5 ns whereas the slow shaper is optimized for energy resolution with ENC¹ of 12.7 e/pF + 233 e and a peaking time of the order of 100 ns. A comparator in each channel is connected to a fast shaper output and the common threshold reference level. It reacts to negative or positive signal respectively to the polarity bit setting in the control logic. If the signal's amplitude triggers the discriminator, its output latches the current time-stamp value and stores it into the 4-words deep Digital FIFO². Simultaneously, the Peak-Hold-Detector is detecting the amplitude³ and storing it in another 4-word deep analogue FIFO. Every channel can be masked and thus is not delivering data to the back-end, whereas the channel itself is working in his normal way. The average per channel hit rate is 160 kHz with 10 % dead-time.

All the channels are connected then to a common Token Manager device which reads channel by channel while checking the status of the FIFO memory, and streams out the data with a frequency of 32 MHz⁴. The energy information is given as an analogue signal and an external ADC is need.

All channels use a common biasing for different parameters of the pre-amplifier, shapers and peak-detectors, controlled by 16 DAC registers. Another set of digital registers control the input polarity and readout modes. The registers are changed via an I²C interface.

The threshold settings for the discriminators is common for all channels. To precisely adjust the individual threshold level each channel has its own trimmer (TrimDAC).

The n-XYTER can operate in 4 modes, dependent on the settings of the two logic bits: *Test Pulse mode* and *Test Trigger mode*.

¹Equivalent Noise Charge, describes the intrinsic noise of the electronics device. The ENC value expresses the number of electrons on the input generating the same output like intrinsic noise does.

²First-In, First-Out

³Peak detector is unipolar and works only with a positive polarity of the signal. In fact the slow shaper is a two stage device, where the first stage can invert the polarity with the polarity bit setting.

⁴This is the frequency of the data frame, each frame consist of 4 words and the data clock is 128 MHz.

When the first bit is set, the rising edge on the External Test Pulse input triggers an internal pulse generator coupled to the channel input via a capacitor. The pulser settings allows to inject a charge in a range of 0fC to 11.1fC (1 MIP \equiv 4fC for 300 μ m thick silicon detectors). This mode can be used to inject the charge to the channel and verify proper working of the front-end stages.

When the second bit is set, the channel discriminator is bypassed forcing the channel to trigger on the External Test Pulse rising edge. Additionally, the status of the discriminator output is stored in the mirror register⁵. In this mode the self-triggering mode of the chip is switched off and the chip works as a triggered device.

All four combinations of testing modes are allowed. When both bits are off, the n-XYTER is working in the default way.

The total current consumption is below 750mA at 3.3V. An individual channel consumes around 10.4mW of power and unused channels can be switched off to decrease power consumption⁶.

6.1.1 Front-End Board

The readout modules for the n-XYTER – FEB (Front-End Board) rev D is shown on fig. 6.2. It is a development module designed for the future STS (Silicon Tracking System) for the CBM experiment. It contains all required parts to fully operate the n-XYTER,

⁵This read-only register is available as a mask register. The peak detector is storing the current value of the slow shaper output. When the Test Trigger mode is on, reading out the mask register will give in fact the status of mirror register.

⁶Switching of the channel influences its neighbourhood (inter-channel capacitances) thus it is recommended to mask unused channels. For this reason, two dummy channels are implemented on both sides of the group of 128 (+1 test channel) channels to provide an equal environment for all channels.

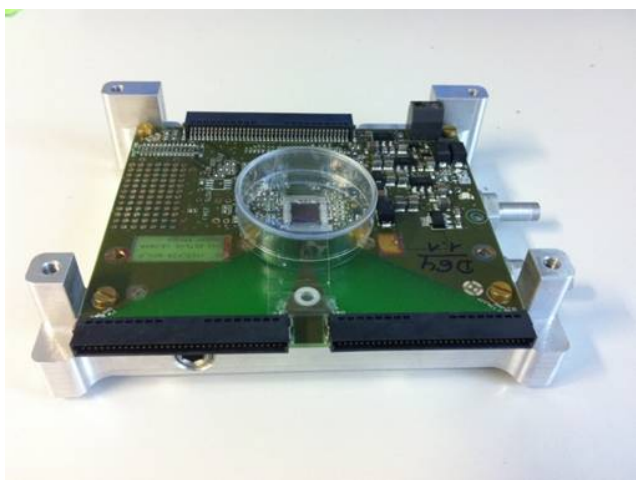


Figure 6.2: The n-XYTER readout module (FEB) together with aluminium water cooling block.



Figure 6.3: The High Voltage and decoupling adapter for the FEB.

including the ADC to digitize the analogue signals from the n-XYTER.

6.1.2 HV Adapter Module

The Adapter module shown on fig. 6.3 is used for detector biasing and signal decoupling. One adapter is used for one side of the detector. The adapter is mounted outside the chamber, between the Detector PCB and the FEB module as it is shown on fig. 5.1.

The adapter as well as the FEB modules should be shielded against environmental noise. This is achieved with the help of a copper box placed around the electronics.

6.1.3 Front-End Cooling

To provide stable operating conditions for the electronics a cooling system is under development. Currently, a water cooling with a radiator cooling is used. In the future active cooling with Peltier modules is planned. The new solution will enable the control of the temperature.

6.2 Integration of the n-XYTER to the HADES DAQ

Figure 6.4 shows an overview of the Cerberus readout for HADES. The system is designed to work standalone with a minimum number of required connections. The data transfer can either be realized by the full-duplex TrbNet⁷ protocol which is then concentrated in a dedicated hub or by gigabit Ethernet (copper or optic links) directly from the TRB3. The trigger is provided by the HADES Central Trigger System (CTS). Slow Control can be implemented in the EPICS server-client framework, although for the pion experiments a stand alone applications will be used.

6.2.1 The TRB3

The integration of the n-XYTER into the Data Acquisition System (DAQ) of HADES is realized by using the *TDC Readout Board version 3 (TRB3)* [21] (fig. 6.5). The main components of the TRB3 are five FPGAs:

⁷The network protocol used by the HADES DAQ.

four peripheral connected to user ports, and one central FPGA for inter-FPGA and TrbNet communication.

6.2.2 n-XYTER Front-End Firmware

The peripheral FPGA is loaded with a firmware for the n-XYTER operation which fulfils the following tasks:

- data readout of the n-XYTER,
- I²C and SPI interfaces for the FEB operation,
- trigger and event building logic,
- TrbNet implementation.

The n-XYTER and the ADC data from the FEB are stored in the internal buffer as hit data where every hit is marked with global time-stamp⁸. To select the data for event building, the event window defined as a window offset and width in respect to the trigger time-stamp is set. All hits with time-stamps within this window are transported and combined to events and sent to the event builders. Each hit contains the relative time-stamp, the channel number, the value of the pulse height and status flags.

6.2.3 The Current Stage of Development

An adapter card has been developed capable of connecting two n-XYTER front-end boards to a peripheral FPGA of the TRB3. Up to four of these cards can be plugged to one TRB3 which allows a total of eight n-XYTER FEEs to be read out via one TRB3.

The following modules are implemented in a VHDL design (firmware) of the peripheral FPGA:

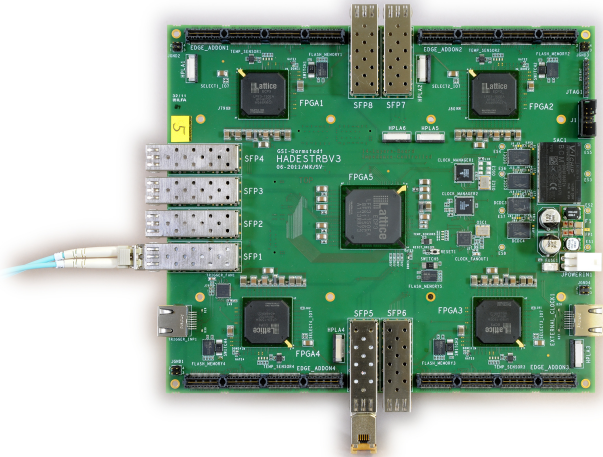


Figure 6.5: The TRB3. One central FPGA and four I/O FPGAs provide a flexible readout system.

1. clock management – to drive the n-XYTER internal structure, synchronise data communication and time-stamps and extend the n-XYTER's 14 bits (4 μ s period) of internal time-stamp,
2. the n-XYTER bus communication – eight data lines, data and frame clock, one data packet contain four data words (one frame),
3. FIFO buffer for n-XYTER data storage,
4. an I²C and a SPI interface for n-XYTER, EEPROM and ADC control (thresholds, channel management, temperature and bias control) and SPI for the ADC (the pulse height information),
5. the trigger and event logic,
6. the TrbNet Slow Control for components configuration.

⁸Extension of only 14-bits long n-XYTER time-stamp.

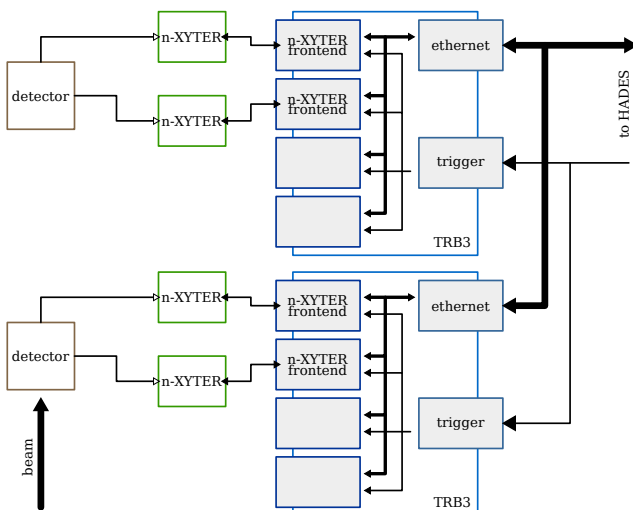


Figure 6.4: The TRB3 readout scheme for Cerberos in HADES.

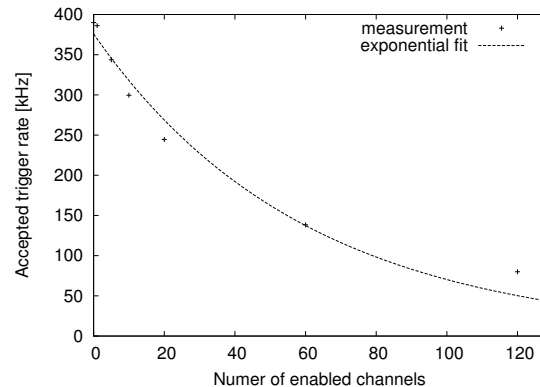


Figure 6.6: Rate measurement of the TRB3+CTS configuration with one n-XYTER front-end for a different number of enabled channels.

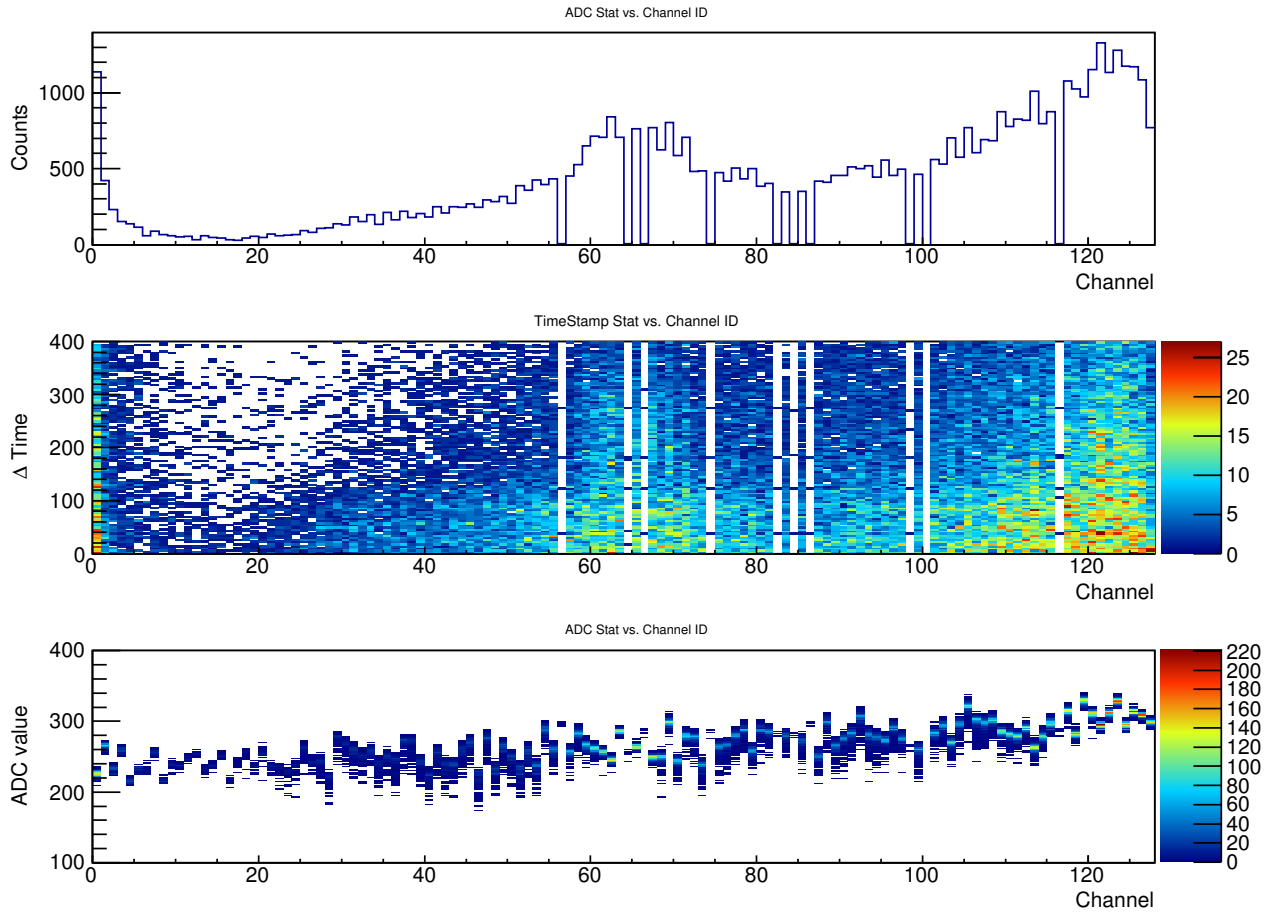


Figure 6.7: Example of data captured with the n-XYTER and the TRB3. The thresholds were set to a low value to trigger on noise. The event timing window was set to 400 ns – middle figure. The upper figure shows the total hit multiplicity per channel, the lower figure show the base line (noise) shape.

6.2.4 Readout/DAQ Performance Test

The performance of the readout has been measured with a high trigger rates and a high data multiplicity. The n-XYTER was put into the Test Trigger mode and the CTS was submitting triggers at a rate of 50 MHz. For different measurements different numbers of channels were enabled. In fig. 6.6 the accepted trigger rate of the CTS as a function of the number of fired channels is plotted. This plot includes the total dead-time of the whole system. With all channels enabled and operated with the maximum trigger rate the data rate resulted in 80 kHz. In normal operation not all channels are firing at the same time, thus, with less than 40 channels firing concurrently the system can run with more than 100 kHz which is sufficient for the anticipated hit rates during the pion experiment.

Figure 6.7 shows an example of data taken in the default mode with one n-XYTER. The thresholds of all channels were set to a low value and noise triggered the hits. The event window is set to 400 ns.

Chapter 7

Beam Results

7.1 General readout test at FOPI@GSI

In October and November 2012 the full detector readout chain was tested at GSI in the FOPI cave. There were several goals for this experiment:

1. Measurement of detector performance – detection efficiency.
2. Measurement of readout performance – efficiency under low and high trigger rate.

The setup used during this measurements is shown on fig. 7.1. Two silicon detectors are placed in the row, allowing for particle tracking. Each of the detectors were read by n-XYTER modules and SysCore modules. One of the SysCores was Master, second was Slave. Each of the n-XYTERs read out one detector side. Water cooling for the temperature stabilisation (down to room temperature) of the electronics was used. The detectors were placed inside light-tight metal chambers with an aluminium foil windows on the

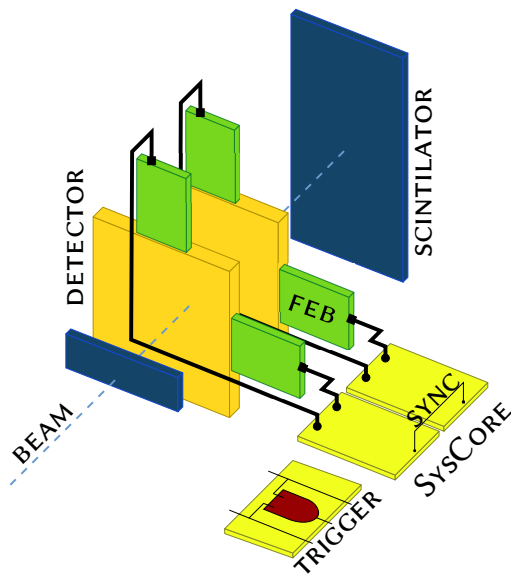


Figure 7.1: DAQ configuration for the 2012 beam time. Two CBM SysCore readout modules were used to read out data from the n-XYTERs.

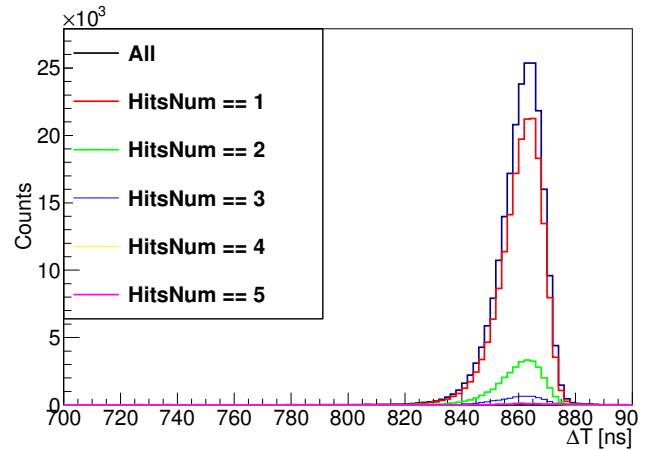


Figure 7.2: Time difference between the silicon hit and the scintillator trigger for different multiplicities of correlated hits. The black curve depicts all the hits, the coloured one shows only hits which belongs to events with certain numbers of fired strips.

particle entrance and particle exit to minimize the material budget.

The trigger was built from the signals of two scintillators placed one on the front and one on the back of the detectors. The trigger signal was connected to a coincidence system and finally three different trigger sources connected to AUX0,1,3 of the Master board were used. Since the SysCore readout was employed during this test, the trigger signal can be used at the unpacking stage. The front scintillator had size of $2 \times 6\text{cm}^2$ and was significantly smaller than the detector area, whereas the scintillator paddle used behind the detectors was much bigger and covered the whole detector area.

Two different projectiles were used as beams: in October the reaction Ni+Al at 1.7 GeV/c energy with two targets 2% and 10% interaction length respectively, and in November the reaction d+Al at 1.9 GeV/c. The first experiment provided high trigger rates and high particle multiplicities, while the latter one was used for low rate particle tracking. Due to the limitation of our DAQ configuration for the high rate beam we were reading out only one detector.

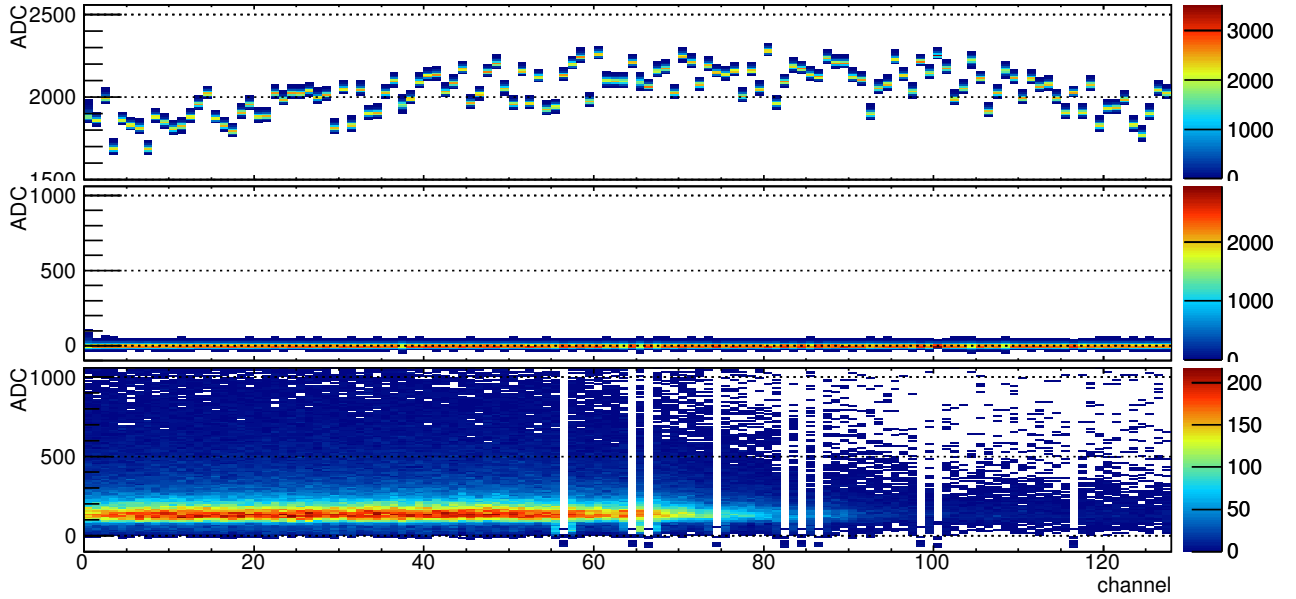


Figure 7.3: Baseline correction. Upper picture show raw noise spectrum (taken in Test Trigger mode). Each channel is fit individual with Gaussian function and mean value is calculated. During data unpacking this mean value is applied as a negative offset to the ADC data. The middle picture one shows noise spectrum after baseline correction, lower picture shows the beam data ADC spectrum with baseline correction.

Detectors were placed ≈ 10 m behind the Al target, thus mostly secondary protons and pions have been measured. To avoid hitting detector with heavier fragments, the detector was placed around ≈ 30 cm away from the beam axis.

7.1.1 Low trigger rate data

Figure 7.2 shows the distribution of the time difference between the silicon hit and the scintillator trigger for the low trigger rate beam (d+Al) for one of the detector sides (all other show similar behaviour). For each event we counted the number of fired strips. We can see that in most of the cases only one fired strip per event is visible, there is some small fraction of events with two fired strips and a negligible fraction of events with higher multiplicity. Multiple hits events are analysed in terms of number of clusters and their sizes. The procedure is described in following.

The time cut 830 ns to 890 ns is applied for data shown at fig. 7.2 to select only correlated hits. All channels within each event are sorted and neighbouring channels are group together to form clusters. The ADC baseline is corrected (fig. 7.3), hence ADC values can be accumulated for each cluster. Figure 7.4 presents distribution of cluster numbers per event and cluster sizes in all analysed events. Figure 7.5 presents the accumulated ADC spectrum of all reconstructed clusters with a data points in blue and fit to the data (red curve), which in this case are mostly MIP particles (protons and pions). The noise (pedestal) spectrum was registered using Test Trigger mode (TTm) as described in section 6.1. Due to correction procedure and TTm

working conditions, 0 ADC in the pedestal spectrum corresponds to negative value of ADC (≈ -40 ADC) in the regular ADC spectrum and after the pedestal correction, the ADC values are shifted in lower values direction. The ADC spectrum was fitted with gauss-convoluted landau distribution[22] thus the peak positions is slightly shifted to higher values with re-

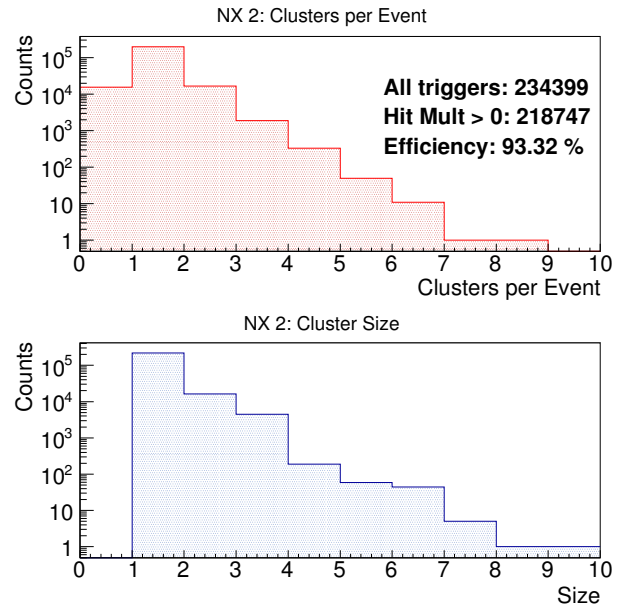


Figure 7.4: Distribution of cluster number (top) per event, and clusters size (bottom). Efficiency given in upper picture is a number of events with at least one cluster.

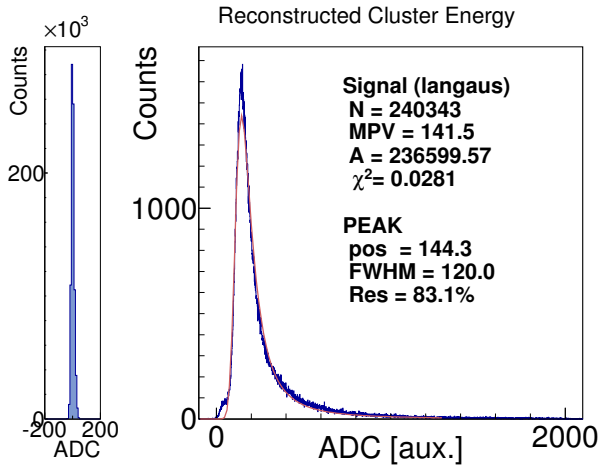


Figure 7.5: Summarized ADC spectrum of all single n-XYTER channels. Red curve shows fit to data. As a reference, the noise peak is shown on the left side.

spect to the Most Probable Value (MPV) of the landau distribution. The energy resolution calculated as $\text{FWHM}/E = 83.1\%$ is rather large¹. The noise peak is not seen there because of internal threshold of the n-XYTER which cuts out the noise. From the smooth shape of the left side of the red plot we can assume that signal separation between noise and signal is good enough that the noise and signal do not overlap. We investigated the signal-to-noise ratio (SNR) defined as $\mu_{\text{ADC}}/\sigma_{\text{noise}}$, where μ_{ADC} is the mean position of the sig-

¹The baseline suppression needs more careful treatment. It is expected that the ADC values will shift to higher values and then the calculated energy resolution will improve. As a reference we assumed 50% from CMS silicon tracker[19].

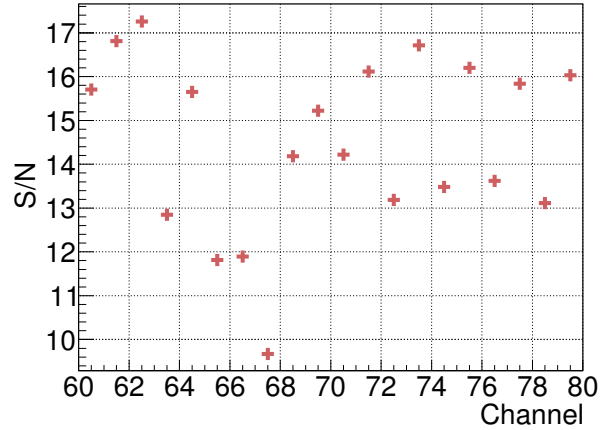


Figure 7.6: Signal-to-Noise ratio for channels 60–80 on the X-side of the front detector (with overlap of trigger scintillator shadow).

nal peak and σ_{noise} is the sigma of the noise peak², for channels which are in geometrical overlap with trigger scintillators. Figure 7.6 shows the SNR for the x-side of the front silicon, calculated as the peak position of the fit function divided by the sigma value of the noise distribution of the channel. The oscillating behaviour of the SNR distribution suggests that a further adjustment of the internal n-XYTER thresholds should be considered.

By selecting only 1-hit clusters for each n-XYTER we can build simplest X-Y correlation distribution of hits on both detectors (fig. 7.7).

The time evaluation of the beam data is shown in

²After applying correction for the 0 position on the ADC spectrum (fig. 7.5) it is expected that SNR value will increase by $\approx 25\%$, though, this correction were not applied.

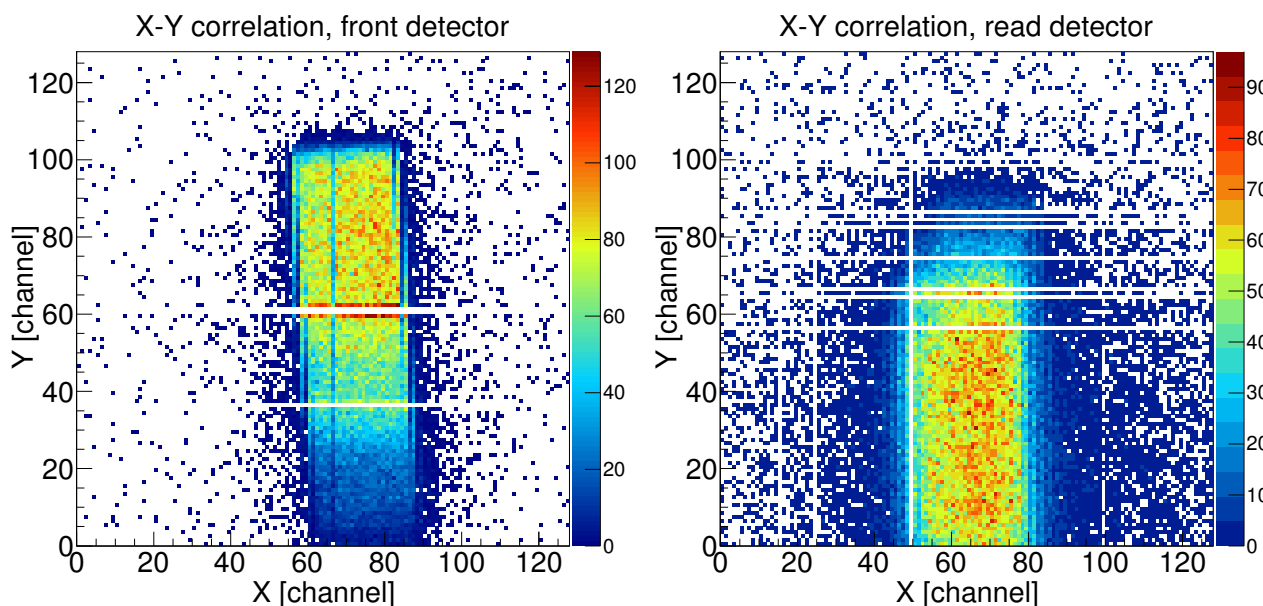


Figure 7.7: Correlation plot between the two detector sides. The left side picture shows the front detector (with respect to the target), the right side shows the back detector. The shadow of the front scintillator is visible.

fig. 7.8. The spill structure of the beam with the beam intensity up to 300 Hz is clearly seen. Detection efficiency was calculated as a ratio of events with at least one detector hit to all registered events (triggers) and average number is on level of 97%. There is very small amount of pileups, and due to low beam rate there are no n-XYTER buffer overflows.

7.2 Beam Results conclusions

The beam tests shown that n-XYTER is capable of stable work for long time under the beam condition. With

its threshold settings it was possible to effectively separate signal from noise, with noise rate (uncorrelated triggers caused by noise) at level of \sim Hz (total number of hits in all channels within the trigger window divided by real measurement time (number of events times window length)). There are no observed effects on signal cutting by threshold settings.

For the effective separation of the signal from noise, the threshold value should be not set lower than $5\sigma_{\text{noise}}$ and thus required value of SNR should be higher than 5. With current result of 14 we are still in the safe range for operation. However, the experimental con-

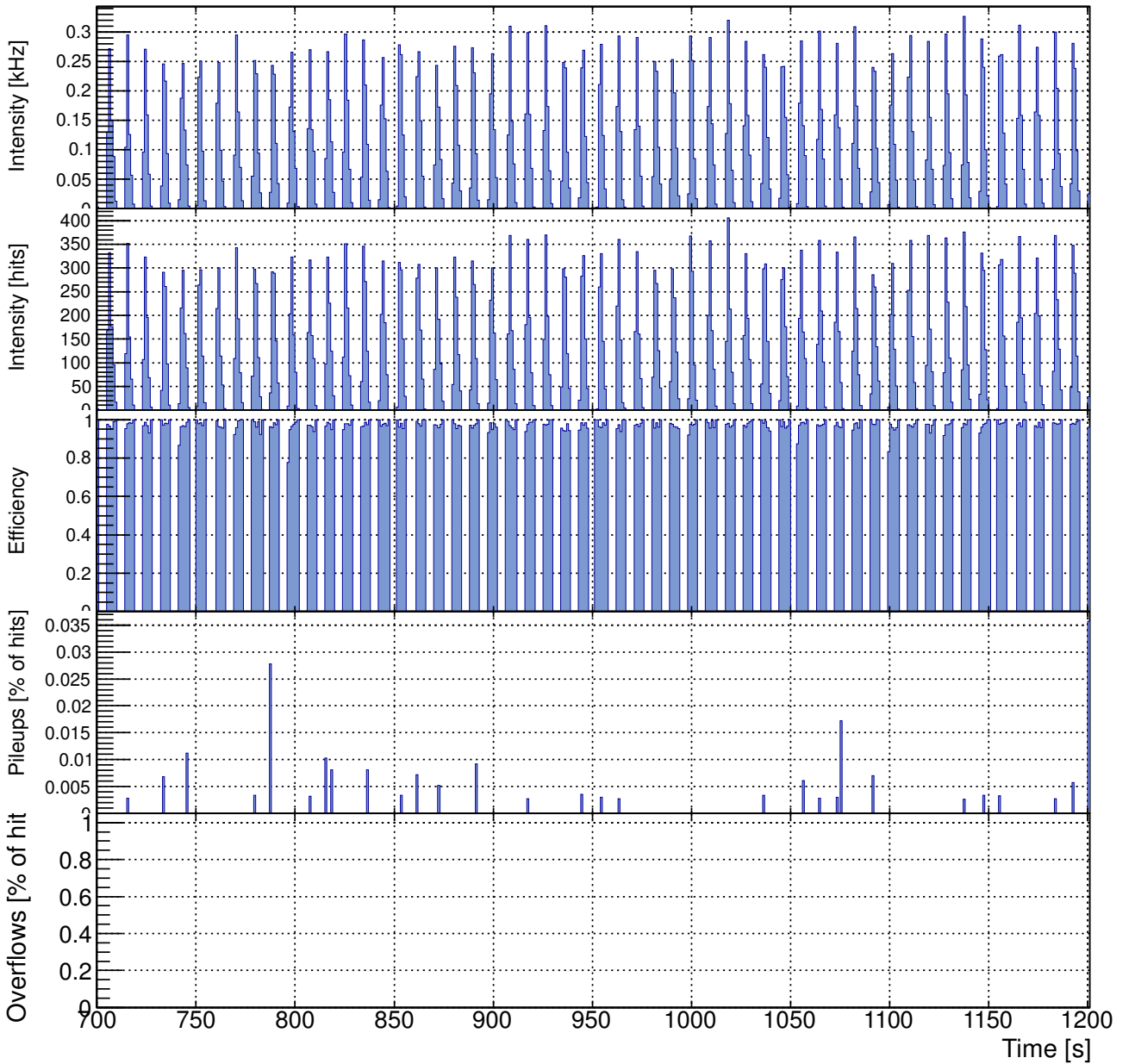


Figure 7.8: Trigger rate, hit multiplicity and detector performance as a function of the time. The upper picture show the trigger rate on period of 500s with binning of 1s. The other distributions from the top show the number of hits for one n-XYTER, detection efficiency, number of pile-ups (as a ratio of all hits) and the number of buffer overflows (also as a ratio of all hits) as a function of the time respectively.

dition were much better than expected, noisy environment of NE5 area. Therefore further optimisation of the shielding and grounding, and further tests in NE5 area are required.

The detector has been tested under low particles rate beams. The high intensity tests were not possible with readout controller SysCore used at that time.

Chapter 8

Start Detector

8.1 Diamond Start Detector Array

A start detector for the pion beam experiments has to fulfil the following requirements:

1. Good time resolution of at least 100 ps for particle identification via time-of-flight.
2. High rate capability of $> 10 \times 10^6 \text{ cm}^{-2} \text{ s}^{-1}$ and corresponding radiation hardness.
3. High efficiency for MIPS of close to 100 %.
4. Low material budget and a position close to the target to minimize the load on the RICH photo-electron detector.
5. Reasonable tracking resolution of $< 1 \text{ mm}$ (sigma) for vertex reconstruction at low reaction multiplicities (supporting the Si tracker).

Mono-crystalline diamonds have been proven to fulfil all these requirements in tests with proton beams[23]. The observed upcharging problems at high rate-densities above $10 \times 10^6 \text{ mm}^{-2} \text{ s}^{-1}$ due to Schottky like, non ohmic contacts resulting in frequent sudden discharges should not be a severe problem for pion beams since the rate density of the pion beam is two orders of magnitude below the critical value. However we are currently investigating systematically the transition to ohmic contacts by forming a thin layer of metal-carbide at high temperatures above 700°C . This work is done in close collaboration with the detector and target laboratories at GSI. An additional boundary condition is the operation inside the liquid hydrogen target-support pipe at a pipe temperature of about 50 K. This limits the heat dissipation to several 10 mW and requires super-isolation surrounding the diamond support boards.

8.2 Start detector design

The following figure shows the design of a 9 element diamond array consisting of two support boards containing 5 and 4 diamonds respectively. The size of each

diamond is between $4.6 \times 4.6 \text{ mm}^2$ and $4.7 \times 4.7 \text{ mm}^2$. In order to achieve a reasonable position resolution and low capacitance each diamond is metalized with 4 quadrants read out separately by a preamplifier based on a high gain, very low noise SiGe:C RF-transistor. A thickness of $300 \mu\text{m}$ is chosen as a compromise between multiple scattering and signal-to-noise ratio at small rise times. The 36 preamplified signals are read out via Cu lines embedded into the support rods (not shown in fig. 8.1). Further amplification and signal shaping is done by an external booster/shaper module outside the vacuum. Final signal discrimination uses a board containing the NINO amplifier/discriminator chip with 8 channels[24] connected to a standard HADES TDC board (TRB2 or 3). The latter chain was used as start detector readout already in previous experiments. According to simulations (tuned to fit previous measurements) the following parameters can be obtained:

1. rise time(10%–90%): 1.35 ns
2. signal/noise ratio: 30:1
3. expected resolution: $< 100 \text{ ps}$
4. preamplifier power consumption:
1.65 mW/channel in total: 60 mW
5. horizontal and vertical pixel resolution (sigma):
0.7 mm each

Since the preamplifier as well as the shaper/booster module is built out of discrete components, above mentioned parameters can be easily tuned.

8.3 Current Status

10 mono-crystalline diamonds are delivered. Two diamonds were metalized and bonded to test boards containing the preamplifiers arranged in the same way as the final version. Two booster/shaper modules were equipped with components and tested. Tests were performed with alpha and beta sources (Am, Sr) as well as with a 26 MeV proton beam to investigate signal shapes and possible upcharge effects. Stable operation at the

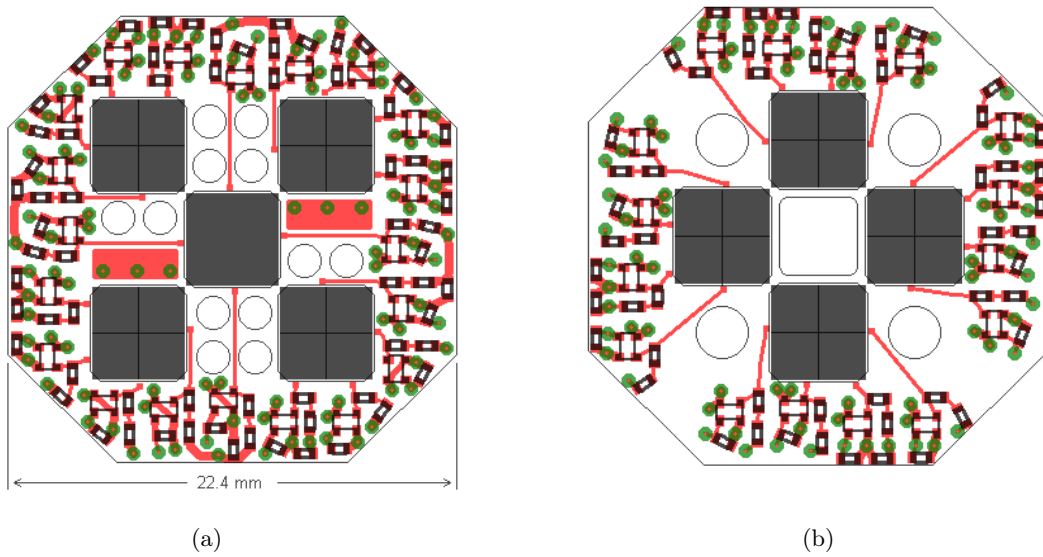


Figure 8.1: Top view of the two diamond support plates containing (a) 5 and (b) 4 diamond detectors (dark grey). The Cu lines are shown in red, the amplifier components as black frames.

desired rise time and pulse height was achieved. However, distinct upcharge effects were observed in particular for alpha particles stopped close to the surface. This effect can reduce the intrinsic field in the bulk material down to nearly zero and results in large signals with opposite polarity once the high voltage is reduced to zero. The decay constant for this reversed field is of the order of several minutes. For electrons and protons punching through the detector, the effect is less pronounced. With the Sr source an amplitude reduction of 20% was observed. The different behaviour indicates that the electron-hole tube produced by particles punching through the detector results in discharge of charge being accumulated below the surface before. Due to large multiple scattering of electrons from a Sr source a significant fraction of these electrons will not punch through. The 26 MeV protons on the other hand were far from MIPs. Thus, a test with a high energy electron beam of 75 MeV will be performed at the S-DANILAC at the TU Darmstadt in October in order to check the detector performance for MIPS behaving very close to a pion beam. In parallel a project has started in collaboration with the GSI detector and target laboratories to check systematically the development of ohmic contacts by high temperature baking of metalized diamonds in a clean vacuum at temperatures above 700 °C. First results showed that metalized diamond material survived tempering at 800 °C for several min. Currently the vacuum in the heating chamber is improved to minimize damage from the residual gas. According to literature [25] ohmic contacts between the metal (e.g. Cr) and the diamond should be established at this temperature avoiding upcharge effects due to Schottky diode behaviour. In parallel the additional heat-load onto the LH2 target was investigated

by insertion of a dummy start detector device as a heat source. An injected heat of up to 300 mW did not effect stable operation of the LH2 target. This shows that a position even closer the LH2 target (currently 40 cm) is feasible and would improve tracking of beam particles needed for vertex reconstruction as well as simplifying the rejection of pions not hitting the fiducial volume of the target.

Bibliography

- [1] G. Agakishiev et al. The High-Acceptance Di-electron Spectrometer HADES. *Eur.Phys.J.*, A41: 243–277, 2009. doi: 10.1140/epja/i2009-10807-5.
- [2] M.L. Benabderrahmane et al. Measurement of the in-medium K^0 inclusive cross section in π^- -induced reactions at 1.15-GeV/c. *Phys.Rev.Lett.*, 102:182501, 2009. doi: 10.1103/PhysRevLett.102.182501.
- [3] V. Koptev et al. Forward K^+ production in sub-threshold pA collisions at 1.0-GeV. *Phys.Rev.Lett.*, 87:022301, 2001. doi: 10.1103/PhysRevLett.87.022301.
- [4] M. Hartmann, Yu.T. Kiselev, A. Polyanskiy, E. Ya. Paryev, M. Buscher, et al. Momentum dependence of the phi-meson nuclear transparency. *Phys.Rev.*, C85:035206, 2012. doi: 10.1103/PhysRevC.85.035206.
- [5] R. Muto et al. Evidence for in-medium modification of the phi meson at normal nuclear density. *Phys.Rev.Lett.*, 98:042501, 2007. doi: 10.1103/PhysRevLett.98.042501.
- [6] D. Cabrera, L. Roca, E. Oset, H. Toki, and M.J. Vicente Vacas. Mass dependence of inclusive nuclear phi photoproduction. *Nucl.Phys.*, A733:130–141, 2004. doi: 10.1016/j.nuclphysa.2003.12.012.
- [7] C.B. Dover, J. Huefner, and Richard H. Lemmer. Pions in nuclear matter - an approach to the pion-nucleus optical potential. *Annals Phys.*, 66:248–292, 1971. doi: 10.1016/0003-4916(71)90189-8.
- [8] E. Friedman and A. Gal. Kaonic atoms and in-medium K-N amplitudes II: interplay between theory and phenomenology. *Nucl.Phys.*, A899:60–75, 2013. doi: 10.1016/j.nuclphysa.2013.01.016.
- [9] E. Oset and A. Ramos. Dynamically generated resonances from the vector octet-baryon octet interaction. *Eur.Phys.J.*, A44:445–454, 2010. doi: 10.1140/epja/i2010-10957-3.
- [10] Matthias F.M. Lutz, Bengt Friman, and Madeleine Soyeur. Quantum interference of ρ^0 - and ω -mesons in the $\pi N \rightarrow e^+e^-N$ reaction. *Nuclear Physics A*, 713(1–2):97–118, 2003. ISSN 0375-9474. doi: [http://dx.doi.org/10.1016/S0375-9474\(02\)01294-0](http://dx.doi.org/10.1016/S0375-9474(02)01294-0).
- URL <http://www.sciencedirect.com/science/article/pii/S0375947402012940>.
- [11] A. I. Titov and Burkhard Kämpfer. Isoscalar-Isovector Interferences in $\pi N \rightarrow Ne^+e^-$ Reactions as a Probe of Baryon Resonance Dynamics. *Eur. Phys. J.*, A12:217–229, 2001. doi: 10.1007/s100500170030.
- [12] Miklos Zetenyi and Gyorgy Wolf. Dilepton production in pion-nucleon collisions in an effective field theory approach. *Phys.Rev.*, C86:065209, 2012. doi: 10.1103/PhysRevC.86.065209.
- [13] M. Zetenyi and G. Wolf. Baryonic contributions to the dilepton spectrum of nucleon nucleon collisions. *Phys. Rev.*, C67:044002, 2003. doi: 10.1103/PhysRevC.67.044002.
- [14] U. Rohrer. PSI Graphic Transport Framework by U. Rohrer based on a CERN-SLAC-FERMILAB version by K.L. Brown et al, 2007. URL http://aea.web.psi.ch/Urs_Rohrer/MyWeb/trans.htm.
- [15] Mesytec. Welcome to mesytec - detector readout systems, 2012. URL <http://www.mesytec.com/>. Online.
- [16] K. Riechmann, K.T. Knoepfle, and V.M. Pugatch. Pion and proton induced radiation damage to silicon detectors. *Nucl.Instrum.Meth.*, A377:276–283, 1996. doi: 10.1016/0168-9002(95)01408-X.
- [17] G. Lindstrom. Radiation damage in silicon detectors. *Nucl.Instrum.Meth.*, A512:30–43, 2003. doi: 10.1016/S0168-9002(03)01874-6.
- [18] R. Wunstorf, M. Benkert, N. Claussen, N. Croitoru, E. Fretwurst, et al. Results on radiation hardness of silicon detectors up to neutron fluences of 10^{15} -n/cm². *Nucl.Instrum.Meth.*, A315:149–155, 1992. doi: 10.1016/0168-9002(92)90696-2.
- [19] M. Friedl. The CMS silicon strip tracker and its electronic readout. *Doctor Thesis*, 2001.
- [20] AS Brogna, S. Buzzetti, W. Dabrowski, T. Fittowski, B. Gebauer, M. Klein, CJ Schmidt, HK Soltveit, R. Szczygiel, and U. Trunk. NXYTER, a CMOS read-out ASIC for high resolution time and amplitude measurements on high

- rate multi-channel counting mode neutron detectors. *Nuclear Instruments and Methods in Physics Research Section A: Accelerators, Spectrometers, Detectors and Associated Equipment*, 568(1):301–308, 2006.
- [21] M. Traxler, E. Bayer, M. Kajetanowicz, G. Korcyl, L. Maier, J. Michel, M. Palka, and C. Ugur. A compact system for high precision time measurements (< 14 ps RMS) and integrated data acquisition for a large number of channels. *Journal of Instrumentation*, 6(12):C12004, 2011.
- [22] Stefano Meroli. The landau distribution for ionizing particles. Lectures, 2012. URL http://meroli.web.cern.ch/meroli/Lecture_landau_ionizing_particle.html.
- [23] J. Pietraszko, L. Fabbietti, W. Koenig, and M. Weber. Diamonds as timing detectors for minimum-ionizing particles: The {HADES} proton-beam monitor and {START} signal detectors for time of flight measurements. *Nuclear Instruments and Methods in Physics Research Section A: Accelerators, Spectrometers, Detectors and Associated Equipment*, 618(1–3):121–123, 2010. ISSN 0168-9002. doi: 10.1016/j.nima.2010.02.113. URL <http://www.sciencedirect.com/science/article/pii/S0168900210003694>.
- [24] F. Anghinolfi, P. Jarron, F. Krummenacher, E. Usenko, and M. C S Williams. Nino: an ultrafast low-power front-end amplifier discriminator for the time-of-flight detector in the alice experiment. *Nuclear Science, IEEE Transactions on*, 51(5):1974–1978, 2004. ISSN 0018-9499. doi: 10.1109/TNS.2004.836048.
- [25] Xiang-Liu Jiang, Fang-Qing Zhang, Ya-Fei Zhang, Wen-Jun Zhang, and Guang-Hua Chen. Transition layers between cvd diamond films and substrates of strong carbide-forming elements: vanadium, chromium, zirconium, and hafnium. In *San Diego'92*, page 145–153. International Society for Optics and Photonics, 1992.